
Analytic model for photometric variation due to starspots on a differentially rotating star

Yasushi SUTO^{1,2}, Shin SASAKI³, Yuta NAKAGAWA¹, and Othman

BENOMAR^{2,4}

¹Department of Physics, The University of Tokyo, Tokyo 113-0033, Japan

²Research Center for the Early Universe, School of Science, The University of Tokyo, Tokyo 113-0033, Japan

³Department of Physics, Tokyo Metropolitan University, Hachioji, Tokyo 192-0397, Japan

⁴National Astronomical Observatory of Japan, Mitaka, Tokyo 181-0015, Japan

*E-mail: suto@phys.s.u-tokyo.ac.jp

Received 2021 December 17; Accepted 2022 May 10

Abstract

We present an analytic model of the lightcurve variation for stars with non-evolving starspots on a differentially rotating surface. The Fourier coefficients of the harmonics of the rotation period are expressed in terms of the latitude of the spot, ℓ_s , and the observer's line-of-sight direction, ℓ_o , including the limb darkening effect. We generate different realizations of multi-spots according to the model, and perform mock observations of the resulting lightcurve modulations. We discuss to what extent one can recover the properties of the spots and the parameters for the differential rotation law from the periodogram analysis. Although our analytical model neglects the evolution of spots on the stellar surface (dynamical motion, creation and annihilation), it provides a basic framework to interpret the photometric variation of stars, in particular from the existing Kepler data and the future space-born mission. It is also applicable to photometric modulations induced by rotation of various astronomical objects.

Key words: general — stars: general

1 Introduction

The last two decades have seen the birth and growth of the space borne photometry due to missions like MOST (Walker et al. 2003), CoRoT (Baglin et al. 2006), Kepler (Borucki et al. 2010) and TESS (Ricker et al. 2014). These instruments provided for the first time long, continuous high-quality photometric data, enabling the detection of thousands of transiting planets, but also opened a new window on the dynamic and evolution of stars. For example, one of the most remarkable achievements of the Kepler space instrument is the discovery that older low-mass stars rotate too fast compared to theoretical expectations (van Saders et al. 2016). This could only be established by the combined analysis of the stellar photometric variability due to spots and to the stellar pulsations (see e.g. Kjeldsen & Bedding 1995; Christensen-Dalsgaard et al. 1996; Chaplin et al. 2010). In general, the study of the rotation-age relation (Skumanich 1972; Kawaler 1988; MacGregor & Brenner 1991) is an important tool to evaluate the age of stars. The rotation also plays an important role on the solar and stellar dynamo (Ossendrijver 2003; Varela et al. 2016), itself believed to be important for sustaining a latitudinal differential rotation.

Observationally, the stellar rotation period can be estimated from a few independent methods. First, one can combine the equatorial rotational velocity from Doppler broadening and the stellar radius. The spectroscopically derived rotation period, however, depends on the assumed model for the turbulence, and also requires the values of the stellar radius and inclination that are not well-determined in general (Kamiaka et al. 2018). Second, the asteroseismic analysis of the stellar pulsation can estimate the rotation period and the stellar inclination simultaneously. The asteroseismology, however, also required various model assumptions in the analysis, and is applicable only to a relatively small fraction of stars that exhibit measurable oscillations (e.g., Appourchaux et al. 2008; Huber et al. 2013; Benomar et al. 2014; Lund et al. 2017; Kamiaka et al. 2018, 2019). Finally, the photometric variation of lightcurves is by far the most widely used method to estimate the stellar rotation period, and has been intensively applied for the Kepler data (e.g., McQuillan et al. 2014; Mazeh et al. 2015; Angus et al. 2018).

The photometric variation is induced by star-spots corotating with the star. If those spots do not dynamically evolve on the stellar surface, it is relatively easy to estimate the stellar rotation period. In reality, however, the spots have individual lifetimes and even move on the stellar surface, and stars are not necessarily rigid rotators (e.g., Donati & Collier Cameron 1997; Barnes et al. 2005; Donati et al. 2010; Roettenbacher et al. 2013; Walkowicz et al. 2013; Brun et al. 2017; Benomar et al. 2018; Basri & Shah 2020). The formation and dissipation

of spots on the differentially rotating stars, therefore, complicate the interpretation of the photometrically estimated rotation period P_{photo} . Furthermore, we cannot exclude a possibility that starspots and stellar pulsations may have similar time scales in some stellar types, even if not so likely.

Properties of spots have been extensively studied in the past literature for the Sun (e.g., Maunder 1904; Zharkov et al. 2005; Mandal et al. 2021), and also for other stars (Morris 2020). Roettenbacher et al. (2013), for instance, achieved a wonderful lightcurve inversion to predict the starspot evolution on Kepler target KIC 5110407. Nevertheless, it is not easy to accurately predict the nature of spots in general. On the other hand, the photometric rotation periods combined with the spectroscopic Doppler broadening have been extensively used to infer the inclination angle of stars hosting planets (Sanchis-Ojeda et al. 2011; Sanchis-Ojeda & Winn 2011; Hirano et al. 2012; Louden et al. 2021; Albrecht et al. 2021), which have profound implications for the spin-orbit architecture of exoplanetary systems (Queloz et al. 2000; Ohta et al. 2005; Sasaki & Suto 2021). Therefore, it is still useful to have parameterized templates for the photometric variation of stellar lightcurves due to non-evolving starspots. This is the purpose of this paper. We present an analytic model of the photometric lightcurves induced by starspots on a differentially rotating stellar surface *assuming that they do not evolve during the finite observing duration*. We compute mock lightcurves based on the multi-spot model, and address how to interpret the measured distribution of peaks in the Lomb-Scargle periodogram in terms of the stellar differential rotation law.

The rest of the paper is organized as follows. We derive the photometric variation pattern due to a single infinitesimal spot in section 2. The resulting lightcurve modulation including the limb darkening effect is expressed in the Fourier series expansion. In section 3, we apply the analytic model for multispots on a differentially rotating star. Then we generate simulated lightcurves adopting the statistical distribution model of the Sun spots, perform the Lomb-Scargle analysis, and examine the information content of the resulting power spectra. Final section is devoted to summary and conclusion of the paper. The Fourier expansion coefficients in our analytic model are given in Appendix.

2 Photometric variation due to a single starspot

As illustrated in Figure 1, we consider a spherical star with radius R_\star , and parameterize a position vector on the stellar surface in terms of its latitude ℓ and longitude φ :

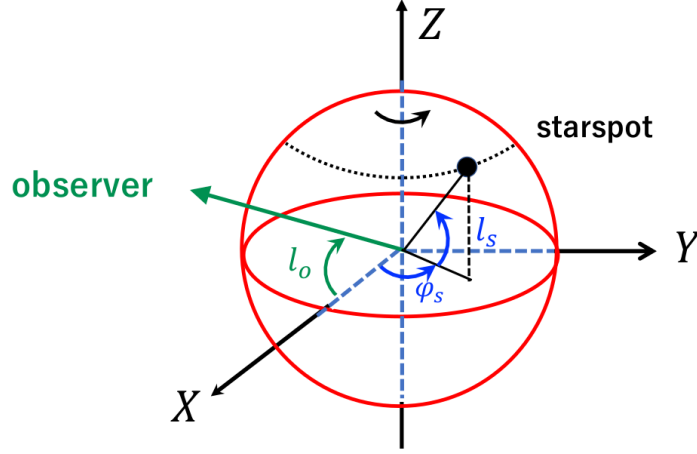


Fig. 1. Schematic illustration of the observer and a starspot. The stellar rotation axis is chosen to be the Z -axis. The location of the spot is specified by the latitude ℓ_s and the azimuth angle φ_s , and the direction of the observer's line-of-sight is defined by the latitude ℓ_o on the $X - Z$ plane ($\varphi = 0$).

$$\mathbf{r}_\star = \begin{pmatrix} x_\star \\ y_\star \\ z_\star \end{pmatrix} = R_\star \begin{pmatrix} \cos \ell \cos \varphi \\ \cos \ell \sin \varphi \\ \sin \ell \end{pmatrix}, \quad (1)$$

where the z -axis is chosen to be the direction of the stellar rotation. In what follows, we assume that the surface angular velocity $\omega(\ell)$ at ℓ is given by the following parameterized model for the latitudinal differential rotation:

$$\omega(\ell) = \omega_0(1 - \alpha_2 \sin^2 \ell - \alpha_4 \sin^4 \ell). \quad (2)$$

For the Sun, $\omega_{0\odot} \approx 2.972 \times 10^{-6} \text{ rad s}^{-1}$, $\alpha_{2\odot} \approx 0.163$, and $\alpha_{4\odot} \approx 0.121$ (Snodgrass & Ulrich 1990). Thus, the angular velocity at $\ell = 30^\circ$ is about 5 percent smaller than its equatorial value.

Without loss of generality, we consider a distant observer located at $\varphi_o = 0$ and ℓ_o . Thus the unit vector toward the observer is

$$\mathbf{e}_o = (\cos \ell_o, 0, \sin \ell_o). \quad (3)$$

According to equation (2), the longitude of the starspot located at the latitude ℓ_s at epoch t becomes

$$\varphi_s(t) = \varphi_{s0} + \omega_s t \quad (4)$$

due to the stellar surface rotation, where φ_{s0} is the longitude at which the spot is located on the stellar surface initially ($t = 0$), and $\omega_s \equiv \omega(\ell_s)$ is the angular velocity of the spot at ℓ_s defined as equation (2).

2.1 A single infinitesimal starspot without limb darkening

A normalized lightcurve of the stellar surface is

$$L(t) = \frac{\int \cos \ell d\ell d\varphi A(\ell, \varphi) K(\ell, \varphi; \ell_o, \varphi_o)}{\int \cos \ell d\ell d\varphi K(\ell, \varphi; \ell_o, \varphi_o)}. \quad (5)$$

where the integration is over the stellar surface, A indicate the surface intensity distribution, and K is the weighting kernel of the surface visible for the observer (e.g., Fujii et al. 2010, 2011; Farr et al. 2018; Haggard & Cowan 2018; Nakagawa et al. 2020).

In the case of a single infinitesimal starspot at (ℓ_s, φ_s) on a homogeneous sphere, we set

$$A(\ell, \varphi) = 1 - \frac{b_{\text{spot}}}{\cos \ell} \delta(\ell - \ell_s, \varphi - \varphi_s). \quad (6)$$

The dimensionless parameter b_{spot} represents the amplitude of the photometric modulation (Dorren 1987; Haggard & Cowan 2018).

Sunspots consist of the central darker part (*umbra*), and the surrounding lighter part (*penumbra*). In addition, there is a type of brighter spots (*faculae*). Note that it is not necessary to specify separately the temperature and area of spots, since the amplitude of the photometric variations of stars depends on their flux (i.e., b_{spot}) alone. As described in §3.2, we consider the spot distribution directly derived from the observed properties using the photometric variation data of the Sun.

Our analytic formulation, however, is general and applicable to various types of spots including umbra, penumbra and faculae ($b_{\text{spot}} < 0$), if we employ their distribution function properly.

Without loss of generality, we can define the initial phase of the single starspot to be $\varphi_s(t=0) = \varphi_{s0} = 0$. For an isotropically emitting stellar surface, the weighting kernel K is equivalent to the visibility computed from the direction cosine $\mu \equiv \mathbf{e}_o \cdot \mathbf{e}_\star$ between the stellar surface $\mathbf{r}_\star = R_\star \mathbf{e}_\star$ and the observer \mathbf{e}_o . The spot is visible (invisible) to the observer if $\mu > 0$ ($\mu < 0$). Thus the weighting kernel is simply computed from equations (1) and (3) as

$$\begin{aligned} K(\ell, \varphi; \ell_o, \varphi_o) &= \max(\mu, 0) \\ &= \max(\cos \ell_o \cos \ell \cos \varphi + \sin \ell_o \sin \ell, 0) \\ &= \cos \ell_o \cos \ell \max(\cos \varphi + \tan \ell_o \tan \ell, 0). \end{aligned} \quad (7)$$

Substituting equations (6) and (7) into equation (5), one obtains a normalized lightcurve modulation due to a single starspot on an otherwise homogeneous spherical surface:

$$L_s(t) \equiv L(t) - 1 = -\frac{b_{\text{spot}} \cos \ell_o \cos \ell_s}{\pi} \max(\tan \ell_o \tan \ell_s + \cos \varphi_s(t), 0). \quad (8)$$

For $\ell_o = \ell_s = \varphi_s(t) = 0$, equation (8) reduces to $L_s(t) = -b_{\text{spot}}/\pi$, and the denominator π indeed corresponds to the visible projected area of the stellar surface πR_\star^2 . Thus, we note that b_{spot} represents the *effective area* of the spot A_{spot} in units of R_\star^2 , instead of πR_\star^2 . Since b_{spot} in equation (6) is defined with respect to the flux, A_{spot} is equivalent to the geometric area of the spot S only when it is completely black. In general, A_{spot} should be interpreted to represent an flux-weighted area of the spot.

In what follows, we adopt a parameterized model of the distribution of A_{spot} that is directly estimated from the observed photometric variations of the Sun (see §3.2). Then we will compute the dimensionless parameter $b_{\text{spot}} \equiv A_{\text{spot}}/R_\star^2$. If the black-body approximation for the stellar surface and the spot is valid, the effective and geometric areas of the spot are related as $A_{\text{spot}} \approx (1 - T_{\text{spot}}^4/T_\star^4)S$ with T_\star and T_{spot} being the temperatures of the star and the spot.

Equation (8) indicates that the starspot is visible at t if

$$\cos \varphi_s(t) + \tan \ell_o \tan \ell_s > 0. \quad (9)$$

For convenience, let us introduce a parameter

$$\Gamma \equiv \tan \ell_o \tan \ell_s. \quad (10)$$

A starspot with $\Gamma > 1$ is always visible to the observer, and equation (8) reduces to

$$L_s(t) = -\frac{b_{\text{spot}} \cos \ell_o \cos \ell_s}{\pi} [\cos \varphi_s(t) + \Gamma]. \quad (11)$$

If $\Gamma < -1$, on the other hand, the starspot is totally invisible and $L_s(t) = 0$.

A starspot with $|\Gamma| \leq 1$ becomes visible periodically as the stellar surface rotation. In this case, equation (8) is expanded analytically in the Fourier series. The result is

$$L_s(t) = -\frac{b_{\text{spot}} \cos \ell_o \cos \ell_s}{\pi^2} \left[(\sin \theta_c - \theta_c \cos \theta_c) + (\theta_c - \sin \theta_c \cos \theta_c) \cos \omega_s t \right. \\ \left. + \sum_{n=2}^{\infty} \left(\frac{\sin(n-1)\theta_c}{n(n-1)} - \frac{\sin(n+1)\theta_c}{n(n+1)} \right) \cos n\omega_s t \right], \quad (12)$$

where the parameter θ_c is defined through $\Gamma = \tan \ell_o \tan \ell_s \equiv -\cos \theta_c$ ($0 < \theta_c < \pi$); see Appendix 1 for the derivation of equation (12).

The visibility of a single starspot is determined by the parameter Γ or equivalently θ_c . We plot the contours of Γ and θ_c on $\ell_o - \ell_s$ plane in the left and right panels of Figure 2, respectively. For a roughly edge-on view observer ($|\ell_o| \ll 1$), spots located near the equatorial plane ($|\ell_s| \ll 1$) correspond to $|\Gamma| \approx |\ell_o \ell_s| \ll 1$, and $\theta_c \approx \pi/2 + \ell_o \ell_s$.

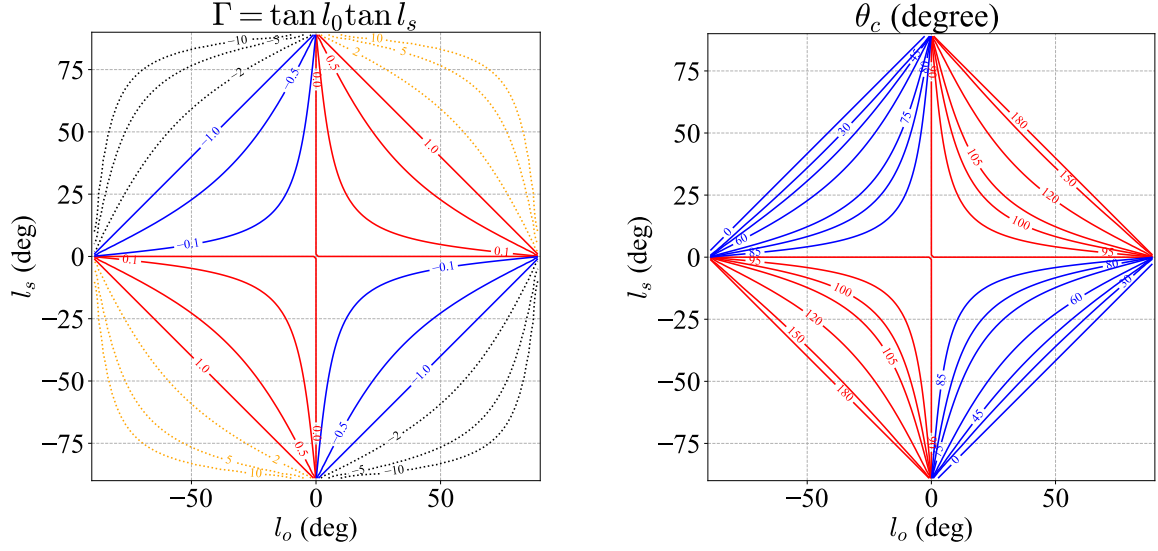


Fig. 2. Contours of $\Gamma (\equiv \tan \ell_o \tan \ell_s)$ and $\theta_c (\equiv -\cos^{-1} \Gamma$ for $|\Gamma| < 1$) on $\ell_o - \ell_s$ plane. Red and blue solid lines in both panels indicate contours for $0 \leq \Gamma \leq 1$ ($90^\circ \leq \theta_c \leq 180^\circ$) and $-1 \leq \Gamma < 0$ ($0^\circ \leq \theta_c < 90^\circ$), for which the corresponding starspot becomes visible periodically to the observer as the star rotates. The orange and black lines correspond to those spots that are always visible and invisible to the observer, respectively.

2.2 A single infinitesimal starspot with limb darkening

The stellar limb darkening produces an additional modulation to the photometric variation due to the starspot. Adopting the quadratic limb darkening law, the normalized stellar surface intensity at \mathbf{r}_\star is characterized by the two limb darkening parameters u_1 and u_2 as

$$I(\mu) = 1 - u_1(1 - \mu) - u_2(1 - \mu)^2 = (1 - u_1 - u_2) + (u_1 + 2u_2)\mu - u_2\mu^2, \quad (13)$$

where $\mu = \mathbf{e}_o \cdot \mathbf{e}_\star$ is the direction cosine that we defined before. We adopt the values of u_1 and u_2 from the Sun (Cox 2000): $u_1 = 0.47$ and $u_2 = 0.23$ at 550 nm (they become 0.42 and 0.23, respectively, at 600 nm).

Including the limb darkening effect, equation (5) is generalized to be

$$L(t) = \frac{\int \cos \ell d\ell d\varphi I(\mu) A(\ell, \varphi) K(\ell, \varphi; \ell_o, \varphi_o)}{\int \cos \ell d\ell d\varphi I(\mu) K(\ell, \varphi; \ell_o, \varphi_o)}. \quad (14)$$

Since the denominator of equation (14) is

$$\begin{aligned} \int \cos \ell d\ell d\varphi I(\mu) K(\ell, \varphi; \ell_o, \varphi_o) &= \int_0^{2\pi} d\phi \int_0^1 \mu d\mu [1 - u_1(1 - \mu) - u_2(1 - \mu)^2] \\ &= 2\pi \left(\int_0^1 \mu d\mu - u_1 \int_0^1 \mu(1 - \mu) d\mu - u_2 \int_0^1 \mu(1 - \mu)^2 d\mu \right) \\ &= \pi \left(1 - \frac{u_1}{3} - \frac{u_2}{6} \right), \end{aligned} \quad (15)$$

equation (8) is now written as

$$L_s(t) = -\frac{b_{\text{spot}}}{\pi} \left(1 - \frac{u_1}{3} - \frac{u_2}{6}\right)^{-1} \max(\mu_s, 0) I(\mu_s). \quad (16)$$

where $\mu_s = \cos \ell_o \cos \ell_s (\cos \omega_s t + \Gamma)$.

Similarly to the previous subsection, equation (16) for $|\Gamma| \leq 1$ is expanded analytically in the Fourier series. The derivation is explicitly given in Appendix 1, and the normalized lightcurve modulation including the limb darkening effect is summarized in the following expression:

$$L_s(t) = -\frac{b_{\text{spot}}}{\pi} \left(1 - \frac{u_1}{3} - \frac{u_2}{6}\right)^{-1} \times \left\{ \frac{A_0}{2} + \sum_{n=1}^{\infty} A_n \cos n\omega_s t \right\}, \quad (17)$$

where

$$A_n \equiv (1 - u_1 - u_2)(\cos \ell_o \cos \ell_s) a_n + (u_1 + 2u_2)(\cos \ell_o \cos \ell_s)^2 b_n - u_2(\cos \ell_o \cos \ell_s)^3 c_n, \quad (18)$$

and the coefficients a_n , b_n , and c_n are explicitly given in Appendix 1.

For spots with $\Gamma > 1$, μ_s is always positive, and the corresponding lightcurve is written in the same form as equation (16) by replacing A_n by \tilde{A}_n , which are given in Appendix 2.

Figures 3, 4, and 5 show the trajectories of a single spot on a rotation stellar surface and the corresponding normalized lightcurves $L_s(t)/b_{\text{spot}}$ against $t/P_{\text{spin}}(\ell_s)$ for an observer located at $\ell_o = 0^\circ$, 30° , and 60° , respectively. Black, red, blue and orange curves indicate the results for the spot at the latitude of $\ell_s = 0^\circ$, 15° , 45° , and 75° . Solid and dashed lines in the right panels indicate the lightcurves with and without limb-darkening (LD).

The right panel of Figure 3 shows that the modulation amplitude $|L_s(t)/b_{\text{spot}}|$ without the limb darkening effect becomes $1/\pi$ for $\ell_o = \ell_s = 0^\circ$ (black-dashed curve) at $\varphi_s(t) = 0$. Limb darkening decreases the effective visible area of the entire surface by a factor of $(1 - u_1/3 - u_2/6)^{-1}$, while that of the starspot by a factor of $I(\mu_s)$. Depending on the location of the spot, ℓ_o , ℓ_s , and $\varphi_s(t)$, the resulting $|L_s(t)/b_{\text{spot}}|$ with limb darkening becomes either smaller or larger than that without limb darkening; see Figures 3, 4 and 5.

Figure 6 plots the ratios of Fourier coefficients of the single spot modulation, A_n/A_1 ($n = 2, 3, 4$). If limb darkening is neglected, they reduce to a_n/a_1 that are a function of $\Gamma \equiv \tan \ell_o \tan \ell_s$ (or θ_c) alone, which are plotted in dotted lines. When the limb darkening effect is taken into account, A_n/A_1 depends on both ℓ_o and ℓ_s . As Figure 6 implies, however, difference among the three curves for $\ell_o = 10^\circ$, 30° , and 60° is small. Thus, A_n/A_1 is still largely determined by the value of Γ (or θ_c) even with limb darkening.

This result suggests that A_n/A_1 may be used to examine if the periodic signals detected from the observed photometric lightcurve are due to starspots, instead of other sources. It may be even possible to put a constraint on Γ from A_n/A_1 in principle. Since ℓ_o is equivalent to the

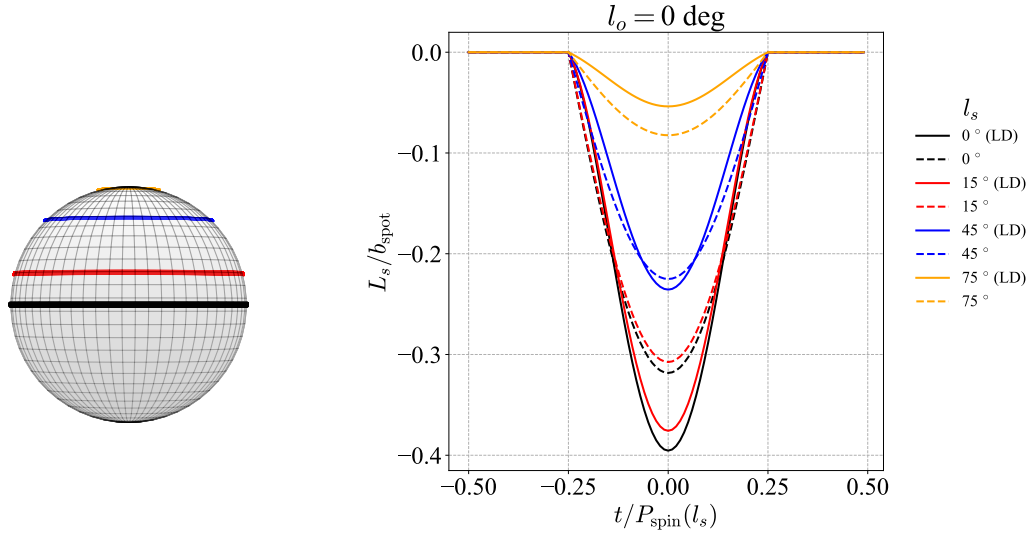


Fig. 3. Photometric modulation due to a single spot at ℓ_s viewed from the observer at $\ell_o = 0^\circ$. *left*: trajectories of four spots at $\ell_s = 0^\circ$ (black), 15° (red), 45° (blue), and 75° (orange) on the stellar surface. *right*: modulation curves L_s/b_{spot} over the one rotation period of each spot $P_{\text{spin}}(\ell_s)$ in the left panel. Solid and dashed lines correspond to those with and without limb darkening (LD) for the differential rotation parameters of $\alpha_2 = \alpha_{2\odot}$ and $\alpha_4 = \alpha_{4\odot}$; see equation (2).

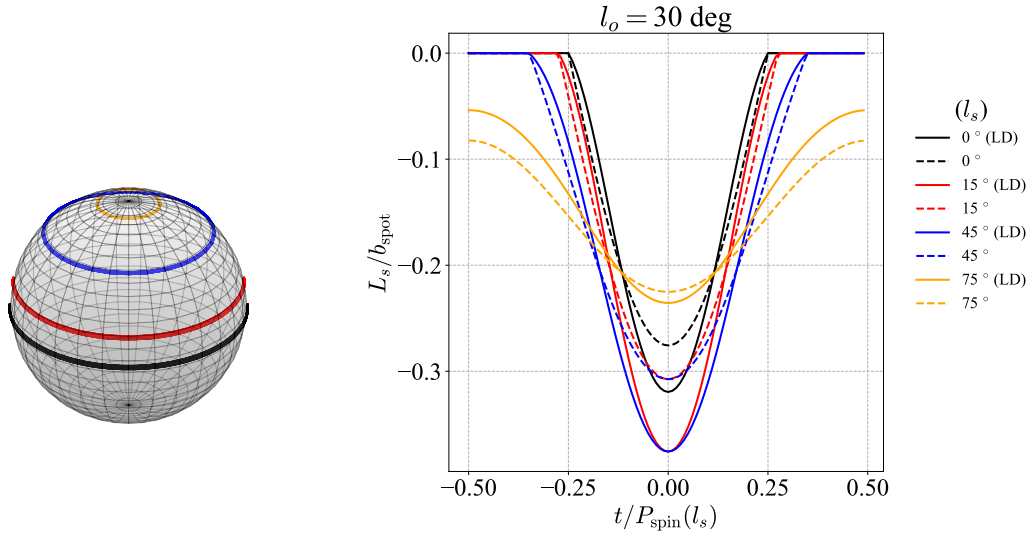


Fig. 4. Same as Figure 3 but viewed from the observer at $\ell_o = 30^\circ$.

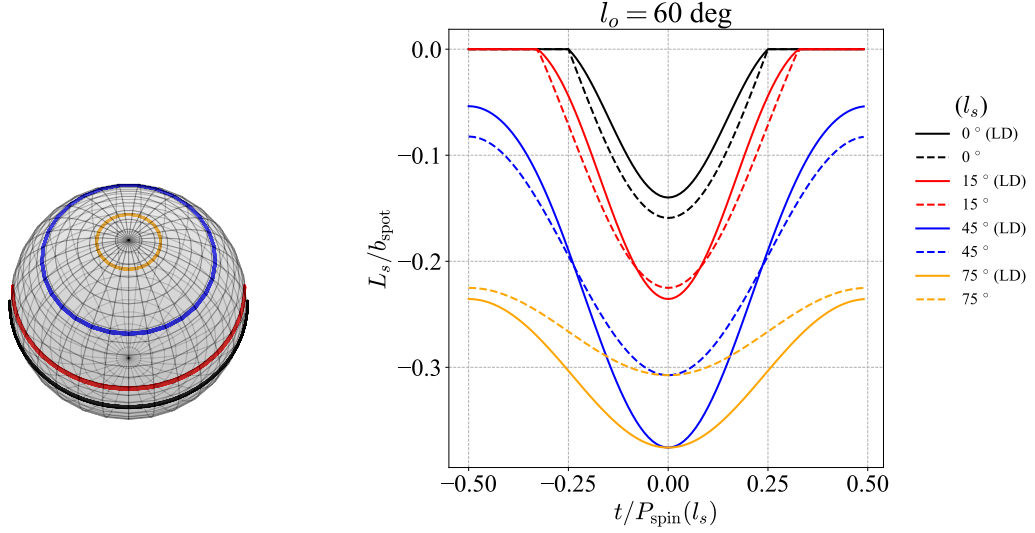


Fig. 5. Same as Figure 3 but viewed from the observer at $\ell_o = 60^\circ$.

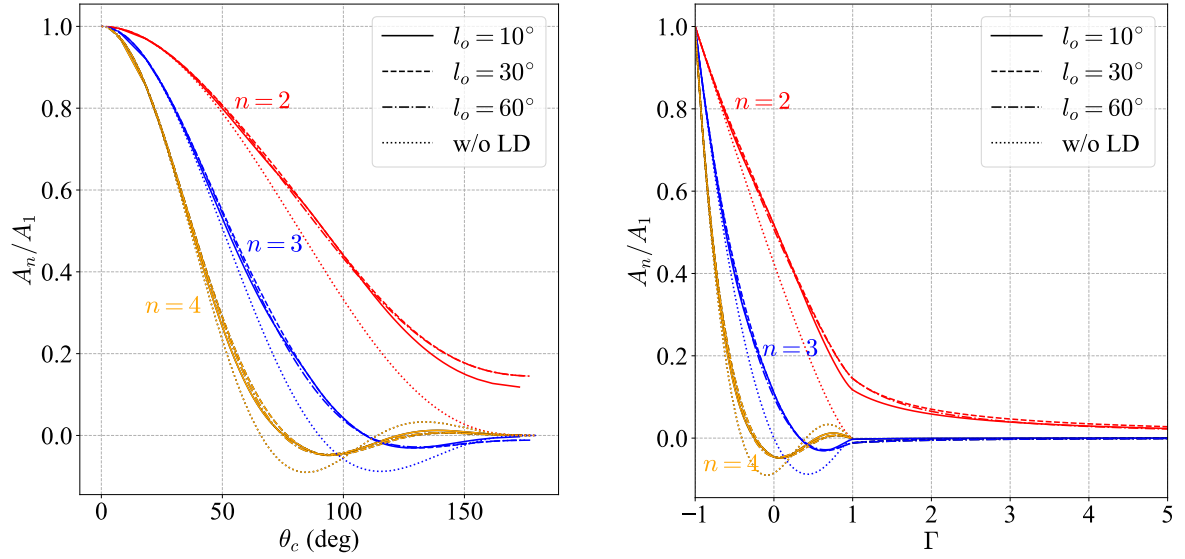


Fig. 6. Ratios of Fourier coefficients of the photometric modulation due to a single spot, A_n/A_1 , plotted against θ_c (left) and Γ (right). Red, blue, and orange lines indicate A_2/A_1 , A_3/A_1 , and A_4/A_1 , respectively. We assume the limb darkening parameters of $\alpha_2 = \alpha_{2\odot}$ and $\alpha_4 = \alpha_{4\odot}$, and plot those ratios in solid ($\ell_o = 10^\circ$), dashed ($\ell_o = 30^\circ$), and dot-dashed ($\ell_o = 60^\circ$) lines. For reference, the results without limb darkening (w/o LD) are plotted in dotted lines.

stellar inclination for the observer that can be independently measured from either spectroscopy or asteroseismology (e.g., Kamiaka et al. 2018, 2019; Sasaki & Suto 2021), the constraint on Γ is translated to that on the spot latitude ℓ_s . In reality, it is feasible to derive a robust constraint on Γ only for a single spot case. The statistical distribution of A_n/A_1 for multi-spots is more useful to constrain the differential rotation as discussed below.

3 Multiple starspots: model predictions and mock data analysis

3.1 Superposition of multiple starspots

If more than one starspots are involved, we have to take into account their relative phases, namely φ_{s0} in equation (4), as well. In that case, equation (17) can be generalized to

$$\begin{aligned} L_s(t) &= -\frac{b_{\text{spot}}}{\pi} \left(1 - \frac{u_1}{3} - \frac{u_2}{6}\right)^{-1} \left[\frac{A_0}{2} + \sum_{n=1}^{\infty} A_n \cos n(\omega_s t + \varphi_{s0}) \right] \\ &= -\frac{b_{\text{spot}}}{\pi} \left(1 - \frac{u_1}{3} - \frac{u_2}{6}\right)^{-1} \left[\frac{A_0}{2} + \sum_{n=1}^{\infty} A_n (\cos n\varphi_{s0} \cos n\omega_s t - \sin n\varphi_{s0} \sin n\omega_s t) \right]. \end{aligned} \quad (19)$$

Thus, the lightcurve due to multispots becomes the superposition of the following form:

$$\begin{aligned} L_s(t) &= -\frac{1}{\pi} \left(1 - \frac{u_1}{3} - \frac{u_2}{6}\right)^{-1} \\ &\quad \times \left\{ \sum_{i=1}^{N_s} b_{\text{spot},i} \left[\frac{A_{0,i}}{2} + \sum_{n=1}^{\infty} A_{n,i} (\cos n\varphi_{s0,i} \cos n\omega_{s,i} t - \sin n\varphi_{s0,i} \sin n\omega_{s,i} t) \right] \right. \\ &\quad \left. + \sum_{i=N_s+1}^{N_s+\tilde{N}_s} b_{\text{spot},i} \left[\frac{\tilde{A}_{0,i}}{2} + \sum_{n=1}^3 \tilde{A}_{n,i} (\cos n\varphi_{s0,i} \cos n\omega_{s,i} t - \sin n\varphi_{s0,i} \sin n\omega_{s,i} t) \right] \right\}. \end{aligned} \quad (20)$$

In the above equation, N_s and \tilde{N}_s denote the number of spots with $|\Gamma| < 1$ and $\Gamma > 1$, respectively, $b_{\text{spot},i}$ is the amplitude of the photometric variation, $\varphi_{s0,i}$ is the initial phase, $\omega_{s,i} = \omega(\ell_{s,i})$ is the angular frequency, and $A_{n,i}$ and $\tilde{A}_{n,i}$ are the Fourier components, of the i -th starspot.

3.2 Mock lightcurves and the Lomb-Scargle power spectra

In order to examine to what extent one can extract the characteristic signature of starspots from photometric stellar lightcurves, we create mock lightcurves in the time domain, and compute the Lomb-Scargle power spectra. Our fiducial set of parameters is listed in Table 1.

The key parameter characterizing the spot in our model is b_{spot} . As described in subsection 2.1, b_{spot} is defined as $A_{\text{spot}}/R_{\star}^2$ in our model. Muñoz-Jaramillo et al. (2015) found that the flux-weighted effective area, A_{spot} , for the Solar spot empirically obeys the Weibull distribution:

$$f(A_{\text{spot}}; k, \lambda) dA_{\text{spot}} = k \left(\frac{A_{\text{spot}}}{\lambda} \right)^{k-1} e^{-(A_{\text{spot}}/\lambda)^k} \frac{dA_{\text{spot}}}{\lambda} \quad (21)$$

from the observed photometric variation over years. The Weibull distribution is written in terms of A_{spot}/λ , the amplitude of the resulting spot modulation is simply scaled to the adopted value of λ .

The expectation value of A_{spot} from equation (21) is

$$\langle A_{\text{spot}} \rangle = \int_{A_{\text{th}}}^{\infty} A_{\text{spot}} f(A_{\text{spot}}; k, \lambda) dA_{\text{spot}} = \lambda \Gamma(1 + \frac{1}{k}), \quad (22)$$

where $\Gamma(x)$ denotes the Gamma function and $\Gamma(1 + \frac{1}{k}) \approx 1.75$ for the solar value of $k = 0.54$.

Also the corresponding cumulative number distribution of A_{spot} exceeding the threshold value A_{th} is

$$P(A_{\text{spot}} > A_{\text{th}}) = \int_{A_{\text{th}}}^{\infty} f(A_{\text{spot}}; k, \lambda) dA_{\text{spot}} = e^{-(A_{\text{th}}/\lambda)^k}. \quad (23)$$

For instance, the top 10 percentile of spots have $A_{\text{spot}} > 1.47\lambda$.

The best-fit values of the two parameters, k and λ , vary for different definitions of spots and different datasets (Muñoz-Jaramillo et al. 2015). For definiteness, we adopt “Sunspot Umbral Area” from the Helio-seismic and Magnetic Imager on the Solar Dynamics Observatory (see their Table 1), and adopt $k = 0.54$ and $\lambda = 2.88 \mu\text{Hem} = 2.88 \times 10^{-6}(2\pi R_{\star}^2)$. It is likely that different stars may have different values of k and λ . Since our model is fully analytical, however, it is readily applicable for other choices. Thus, we fix their values below, and generate mock data for multi-spots.

Equation (22) suggests that a characteristic amplitude of the dimensionless parameter b_{spot} of our spots is

$$\langle b_{\text{spot}} \rangle \equiv \frac{\langle A_{\text{spot}} \rangle}{R_{\star}^2} \approx \Gamma(1 + 1/k) \frac{\lambda}{R_{\star}^2} = 2\pi \left(\frac{\lambda}{1 \mu\text{Hem}} \right) \Gamma(1 + 1/k) \text{ ppm}, \quad (24)$$

where the factor of 2π comes from the fact that λ is given relative to the area of hemisphere (Hem), $2\pi R_{\star}^2$. Thus we can safely neglect the finite size effect of an individual spot, which is consistent with the assumptions of our analytic model, for our adopted value of $\lambda = 2.88 \mu\text{Hem}$.

In order to understand the meaning of equation (24), let us define the effective radius of the spot r_{spot} through

$$A_{\text{spot}} = \pi r_{\text{spot}}^2. \quad (25)$$

Substituting equation (24) into equation (25), one obtains

$$\frac{r_{\text{spot}}}{R_{\star}} = \sqrt{\frac{b_{\text{spot}}}{\pi}} \approx 1.8 \times 10^{-3} \sqrt{\frac{b_{\text{spot}}}{10 \text{ ppm}}} \approx 0.1^{\circ} \sqrt{\frac{b_{\text{spot}}}{10 \text{ ppm}}}, \quad (26)$$

or equivalently

$$r_{\text{spot}} \approx 0.19 R_{\oplus} \sqrt{\frac{b_{\text{spot}}}{10 \text{ ppm}}} \left(\frac{R_{\star}}{R_{\odot}} \right). \quad (27)$$

Equations (26) and (27) correspond to the angular and real size corresponding to r_{spot} in terms of b_{spot} .

We generate N_{tot} spots with b_{spot} following the Weibull distribution, equation (21). We adopted $N_{\text{tot}} = 30$ for definiteness so as to roughly reproduce the Solar spots. The corresponding fraction of spots over the entire stellar surface may be computed from equation (22):

$$F(k, \lambda) = N_{\text{tot}} \frac{\langle A_{\text{spot}} \rangle}{4\pi R_{\star}^2} = 7.6 \times 10^{-5} \left(\frac{N_{\text{tot}}}{30} \right) \left(\frac{\lambda}{2.88 \mu\text{Hem}} \right) \left(\frac{\Gamma(1+1/k)}{1.75} \right). \quad (28)$$

The value of N_{tot} is sensitive to the threshold value A_{th} in identifying a single spot even for the Sun, and moreover is not clear for other stars. Our analytic formulation can be applied to a different choice of N_{tot} in a straightforward manner.

The latitudes of spots ℓ_s are drawn from the isotropic distribution function ($\propto |\sin \ell_s|$) but over the restricted range of $-\ell_{s,\text{max}} < \ell_s < \ell_{s,\text{max}}$. We choose $\ell_{s,\text{max}} = 30^\circ$ as our fiducial value, but consider 75° as well to examine its impact. The initial phases are selected randomly for $0 < \varphi_s < 2\pi$.

For a given value of the observer's latitude ℓ_o , we classify each spot according to $|\Gamma| < 1$ and $\Gamma > 1$, and compute the number of such spots N_s and $\tilde{N}_s (= N_{\text{tot}} - N_s)$, respectively. Then the lightcurve modulation due to those spots is computed from equation (20).

We generate the mock lightcurves with cadence T_{samp} over the duration of T_{obs} . We set the fiducial values as $T_{\text{samp}} = 30$ mins and $T_{\text{obs}} = 90$ days, following the long cadence observation for one single quarter of the Kepler dataset.

Finally, we add the Gaussian noise to the lightcurves:

$$f(x) = \frac{1}{\sqrt{2\pi\sigma_n^2}} \exp\left(-\frac{x^2}{2\sigma_n^2}\right). \quad (29)$$

In what follows, we consider two cases, $\sigma_n = 0$ (noiseless) and $\sigma_n = 35\text{ppm}$ as a typical value for the Kepler data (c.f., Walkowicz et al. 2013; Basri & Shah 2020), for simplicity. Equation (21) implies that the flux modulation induced by a single spot is typically much smaller than the noise:

$$\frac{\langle b_{\text{spot}} \rangle}{\pi} = 10 \left(\frac{1.75\lambda}{5.04 \mu\text{Hem}} \right) \text{ppm}. \quad (30)$$

Thus, in the case of $\sigma_n = 35$ ppm, the clear periodic signal is visible only for a relatively big spot ($A_{\text{spot}} > 5\lambda$, roughly corresponds to the top 10 percentile) or a clustered group of nearby spots.

Figure 7 shows the mock data for two different sets of realizations of starspots ($N_{\text{tot}} = 30$, $\ell_{s,\text{max}} = 30^\circ$) for an observer at $\ell_o = 0^\circ$. The fractional area covered by spots varies from 0.3 to 1.3 times the expectation value of equation (28).

We search for periodic signals of an angular frequency ω :

$$S(t) = S_0 + \sum_{n=1}^{n_{\text{terms}}} (S_{2n-1} \sin n\omega t + S_{2n} \cos n\omega t) \quad (31)$$

embedded in the mock lightcurves (*center panels*) using the Lomb-Scargle (LS) method (Lomb

Table 1. Fiducial parameters for mock lightcurves

symbol	range	note
b_{spot}	$k = 0.54, \lambda = 2.88\mu\text{Hem}$	the Weibull distribution
N_{tot}	30	total number of generated starspots
φ_s	$[0, 2\pi]$	uniform
ℓ_s	$ \ell_s < \ell_{s,\text{max}} = 30^\circ$	$P(\ell_s) \propto \sin \ell_s $
ℓ_o	0°	stellar inclination relative to the observer’s line-of-sight
α_2	$\alpha_{2\odot} = 0.163$	differential rotation coefficient
α_4	$\alpha_{4\odot} = 0.121$	differential rotation coefficient
u_1	0.47	linear limb-darkening parameter
u_2	0.23	quadratic limb-darkening parameter
$2\pi/\omega_0$	10 days	equatorial rotation period
T_{samp}	30 mins	cadence of the observation
T_{obs}	90 days	duration of the observation

1976; Scargle 1982). The conventional LS adopts $n\text{terms} = 1$, and we compute the normalized power spectrum:

$$P(\omega) = 1 - \frac{\chi^2(\omega)}{\chi_{\text{ref}}^2}, \quad (32)$$

where $\chi^2(\omega)$ is the residuals of the fit with χ_{ref}^2 being the reference value for a constant model.

Left panels of Figure 7 plot the spot distribution at $t = 0$ for two different realizations. The area of each circle is plotted in proportion to b_{spot} , and approximately represents the true ratio of the spot area and the entire stellar surface (but neglecting the distortion due to the projection onto the plane). Since those spots span a range of latitudes, the resulting lightcurves (center panels) are not exactly periodic in the time domain due to the latitudinal surface differential rotation. Right panels of Figure 7 plot the corresponding LS power. The highest peaks around 10 days are located over a range of rotation periods spanning $P_{\text{spin}}(\ell_s = 0^\circ)$ and $P_{\text{spin}}(\ell_s = \ell_{s,\text{max}})$ due to the differential rotation. The secondary peaks around 5 days are the second harmonics. The ratios of those amplitudes carry important information on ℓ_s and ℓ_o , and will be discussed later (subsection 3.3) using the LS analysis with $n\text{terms} = 2$.

Our mock data completely neglect the dynamics of spots (their creation and dissipation, and motion on the stellar surface) over the duration of the observation $T_{\text{obs}} = 90\text{days}$, that corresponds to the duration of a single quarter of the Kepler dataset. In order to empirically evaluate the effects of the spot dynamic, we create 10 totally independent realizations drawn from the statistically same spot distribution, and compute each LS power and the average over the 10 realizations. The latter may be interpreted as the average LS power of the entire Kepler

$$l_o = 0 \text{ deg}, N_{\text{tot}} = 30$$

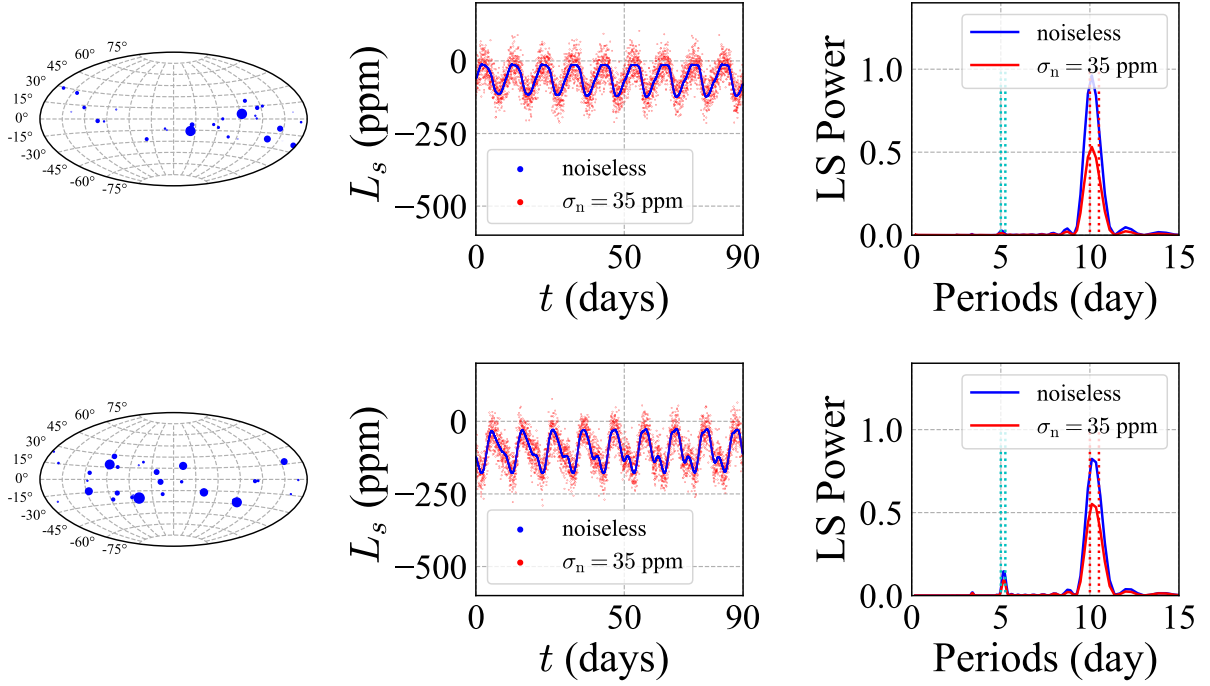


Fig. 7. Lightcurve modulations due to starspots ($N_{\text{tot}} = 30$, $\ell_{s,\text{max}} = 30^\circ$) for an observer at $\ell_o = 0^\circ$. Left, center, and right panels show the spot distribution on the stellar surface, normalized lightcurve, and the corresponding Lomb-Scargle power spectrum. Results for $\sigma_n = 0$ and 35ppm are plotted in blue and red, respectively. Upper and lower panels are different realizations of the statistically same model. The vertical dotted lines indicate the range of the differentially rotation periods; $P_{\text{spin}}(\ell_s = 0^\circ)/2$, $P_{\text{spin}}(\ell_s = \ell_{s,\text{max}})/2$, $P_{\text{spin}}(\ell_s = 0^\circ)$, and $P_{\text{spin}}(\ell_s = \ell_{s,\text{max}})$.

observing period, that is made of up to 10 quarters.

The results are shown in Figure 8. Possible signatures of differential rotation may be found in the variance among the LS power spectra for different quarters. The width of a peak with a detected period is determined by the entire duration of the observation T_{obs} , instead of the cadence T_{samp} in the present examples. For instance, one can resolve the periods for different spots only if they are static over $T_{\text{obs}} = 900$ days, but cannot for $T_{\text{obs}} = 90$ days. While the non-evolving spots over $T_{\text{obs}} = 900$ days may not be so realistic in general, a small fraction of stars may have such spots. Therefore our study suggests that it is worthwhile to attempt searching for such signatures in the Kepler archive data.

Figures 9 and 10 show the same plots as Figures 7 and 8, but for a wider distribution of spots ($\ell_{s,\text{max}} = 75^\circ$) observed from an observer located far outside the stellar equatorial plane ($\ell_o = 45^\circ$). As expected, the effect of differential rotation is more visible than that for $\ell_{s,\text{max}} = 30^\circ$ and $\ell_o = 0^\circ$.

The visible periodicity of the lightcurve modulation in the center panels of Figures 7

$$l_o = 0 \text{ deg}, N_{\text{tot}} = 30$$

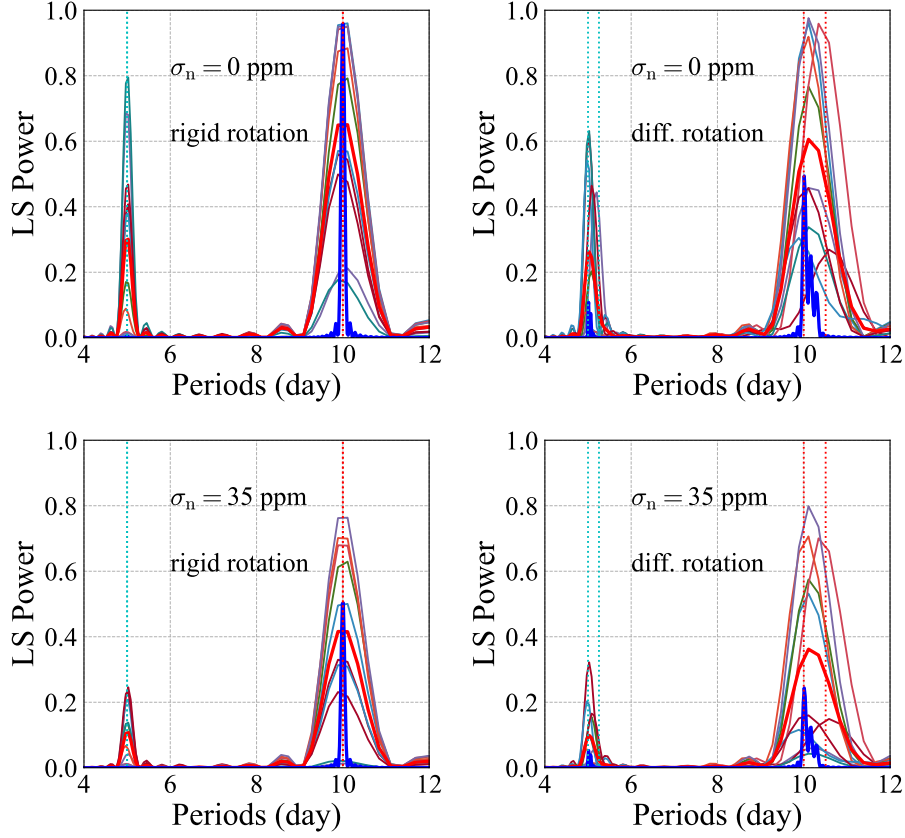


Fig. 8. LS power spectra for different realizations corresponding to Figure 7. Upper and lower panels are for $\sigma_n = 0$ and 35ppm, and left and right panels are without and with differential rotation. Thin curves (10 in total) indicate the results for different realizations of the spots for $T_{\text{samp}} = 30$ mins and $T_{\text{obs}} = 90$ days, with thick red lines being their average. Thick blue lines show the LS power for one realization but observed for $T_{\text{obs}} = 900$ days.

and 9 seems to be generated by a relatively small number of large spots. To clarify this point, we repeated the analysis by dividing the 30 spots in the two realizations of Figures 7 and 9 separately into two groups; the top 10 spots and the remaining 20 spots. The resulting plots are shown in Figures 11 and 12. While those small spots still show periodic signals in the *noiseless* lightcurve, they are substantially buried in the case of our adopted noise of $\sigma_n = 35$ ppm. In other words, the peaks in the LS power spectra are dominated by a small fraction of spots, and should represent mostly their properties (size, latitude, and rotation velocity), as long as the Weibull distribution is a good approximation for the spot distribution for stars other than the Sun. The above result also implies that our basic conclusion is not so sensitive to the choice of N_{tot} ; see Figure 13.

$$l_o = 45 \text{ deg}, N_{\text{tot}} = 30$$

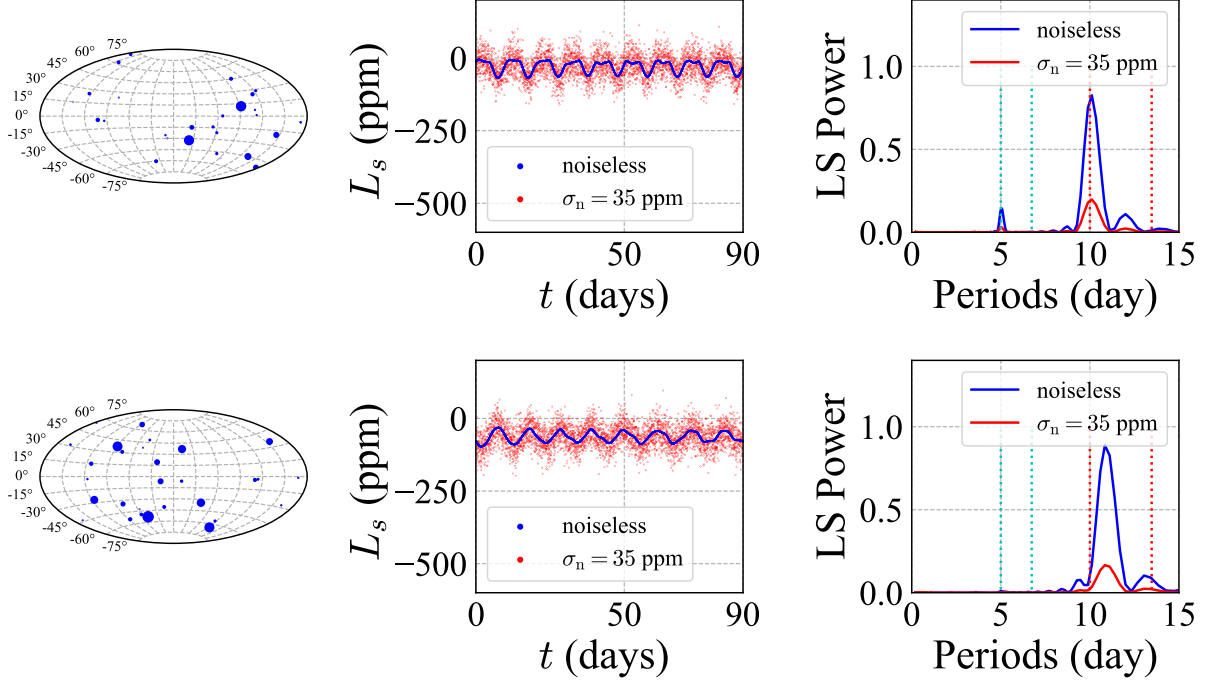


Fig. 9. Same as Figure 7, but for $\ell_{s,\text{max}} = 75^\circ$ and $\ell_o = 45^\circ$.

$$l_o = 45 \text{ deg}, N_{\text{tot}} = 30$$

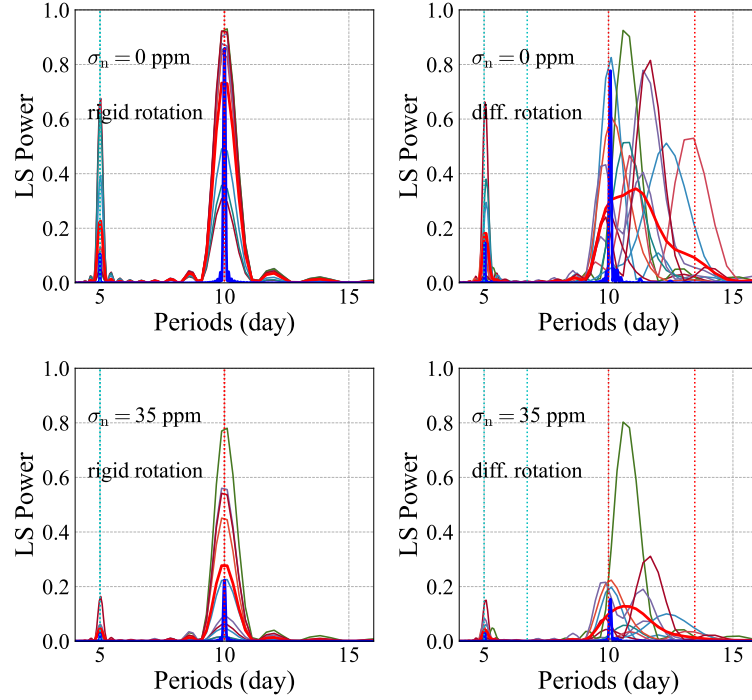
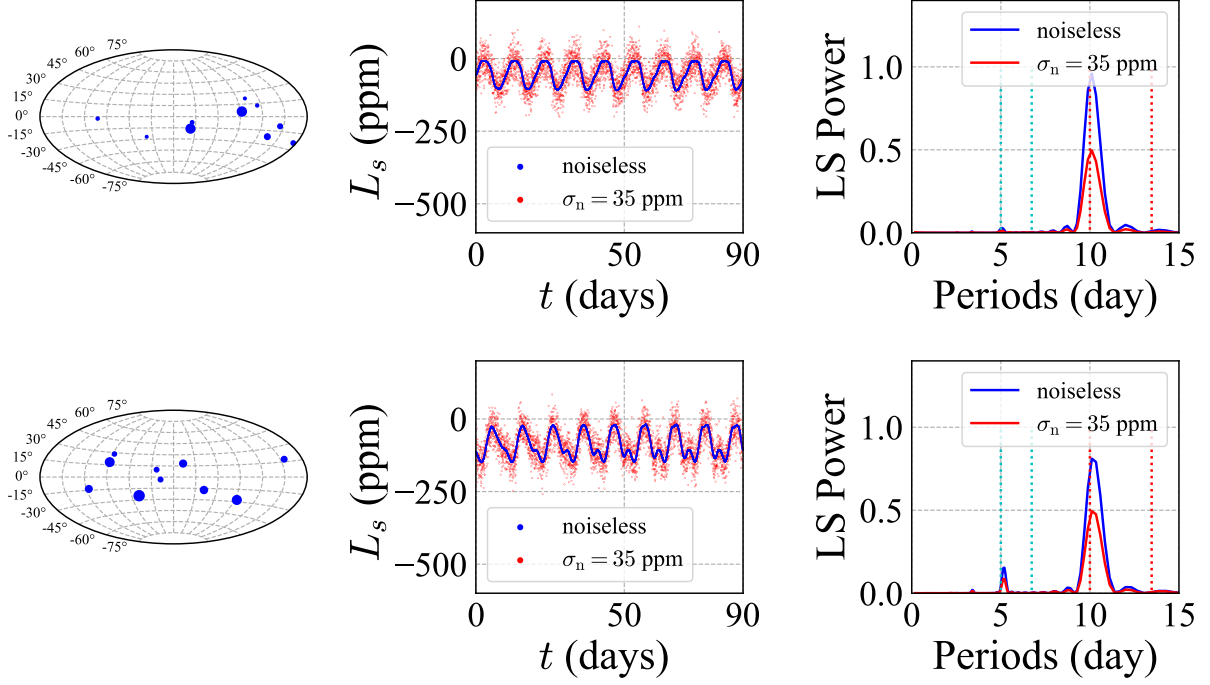


Fig. 10. LS power spectra for different realizations corresponding to Figure 9.

$l_o = 0$ deg, top 10



$l_o = 0$ deg, bottom 20

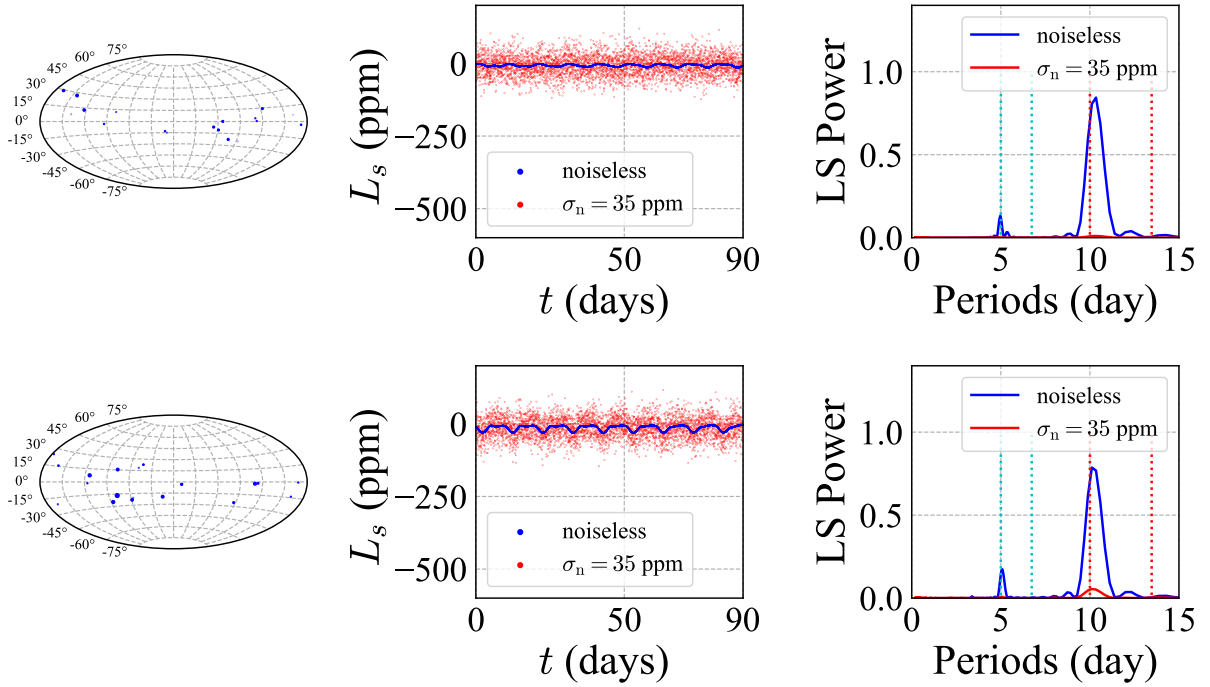
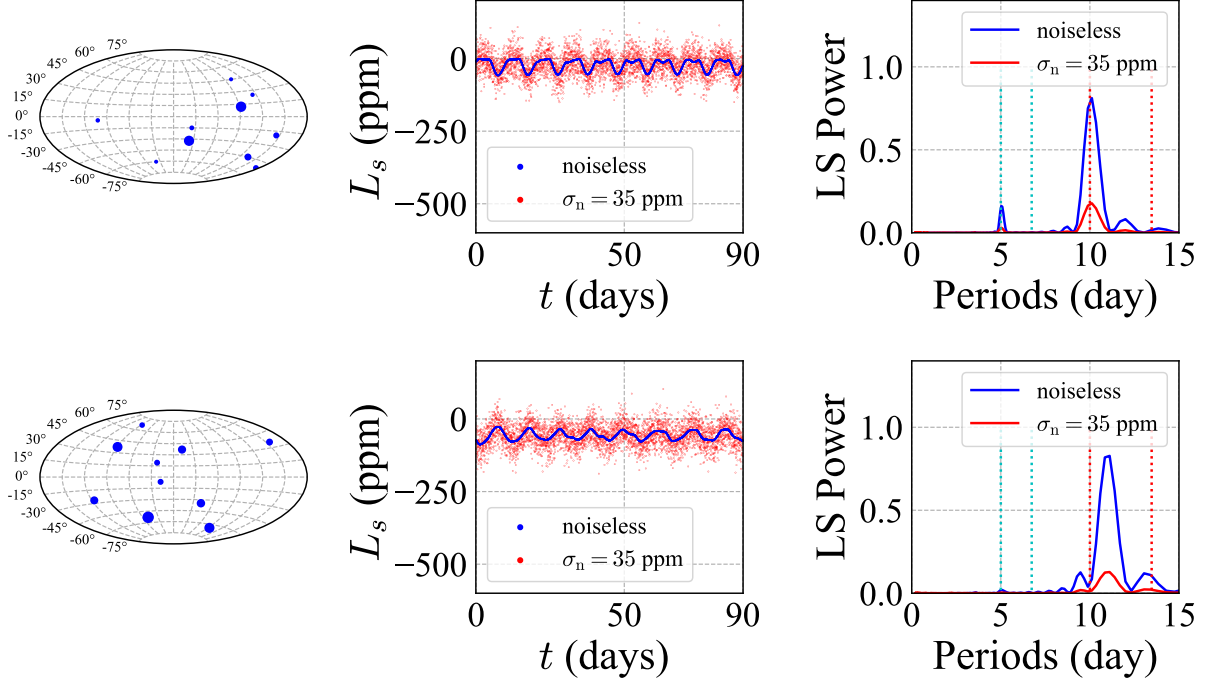


Fig. 11. Same as Figure 7, but computed for the top 10 spots (*upper two panels*) and the remaining 20 spots (*lower two panels*).

$l_o = 45$ deg, top 10



$l_o = 45$ deg, bottom 20

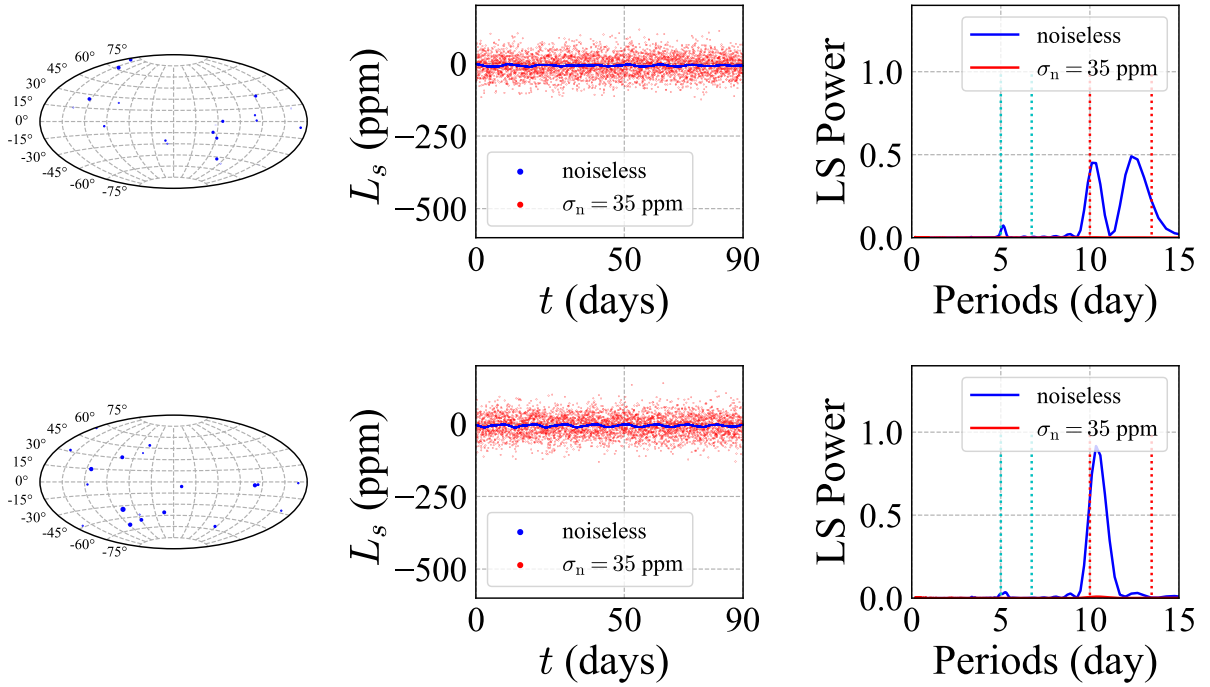


Fig. 12. Same as Figure 9, but computed for the top 10 spots (*upper two panels*) and the remaining 20 spots (*lower two panels*).

$$l_o = 0 \text{ deg}, N_{\text{tot}} = 10$$

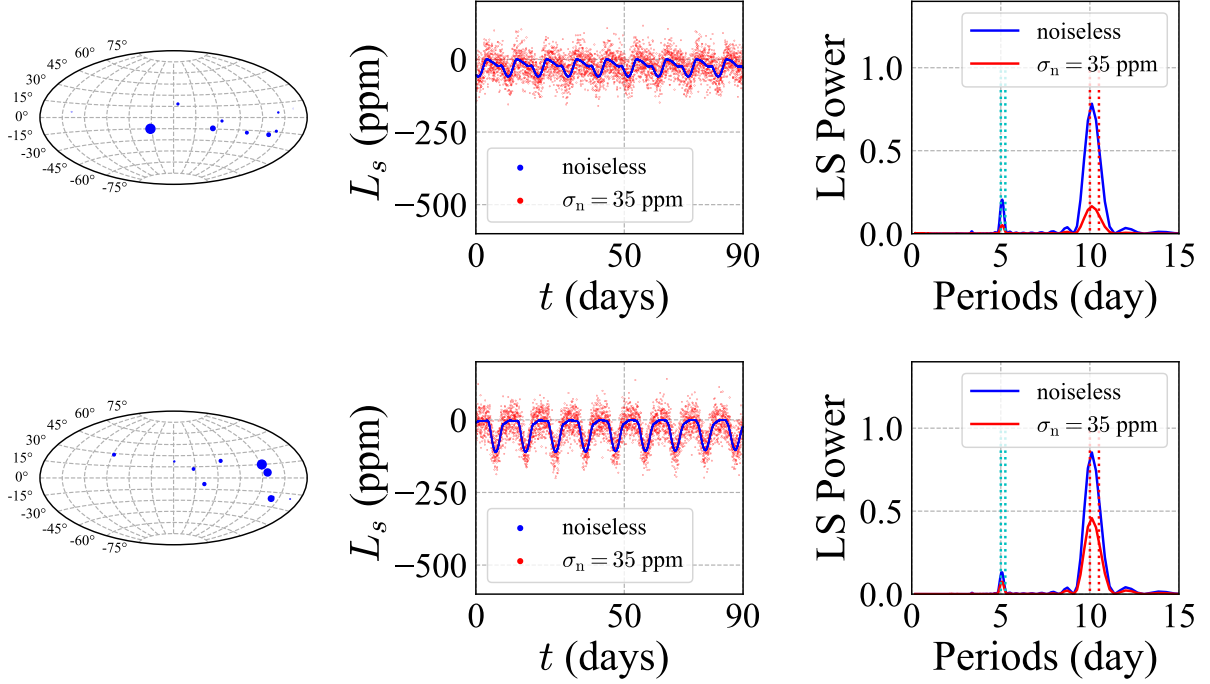


Fig. 13. Same as Figure 7, but for $N_{\text{tot}} = 10$.

3.3 Extracting the spot signature from the amplitude ratios of harmonics

We have shown that a single spot leaves a distinctive modulation pattern in the Fourier coefficients of the harmonics (Figure 6). In principle, the signature is important to distinguish between the true and false rotation periods from photometry. Nevertheless, it may be weakened for more realistic cases of multispots, in particular under the presence of the stellar differential rotation. We consider this question in detail using mock data analysis.

Consider a single spot case. Figure 14 compares the theoretical model predictions $(A_2/A_1)^2$ (solid lines) for the stellar rotation period against the measurement from the mock data for a single spot located at a given ℓ_s viewed from a line-of-sight direction of ℓ_o . We choose the value of $b_{\text{spot}} \approx 85$ ppm so that it corresponds to the top 10 percent of the whole spot distribution, *i.e.*, $A_{\text{spot}} = 4.7\lambda$ from equations (24) and (23). Incidentally, the theoretical curve is invariant with respect to the transformation of $(\ell_o, \ell_s) \leftrightarrow (\ell_s, \ell_o)$ as equation (11) indicates.

We adopt two different estimators. One is based on the standard Fourier power spectrum, and plots the corresponding amplitude ratio P_2/P_1 (left panel). The other is based on the LS analysis. In this case, we first identify the best-fit angular frequency ω_{fit} from the LS power spectra using $n_{\text{terms}} = 1$ in equation (31). Then we fit the data to equation (31) with $n_{\text{terms}} = 2$

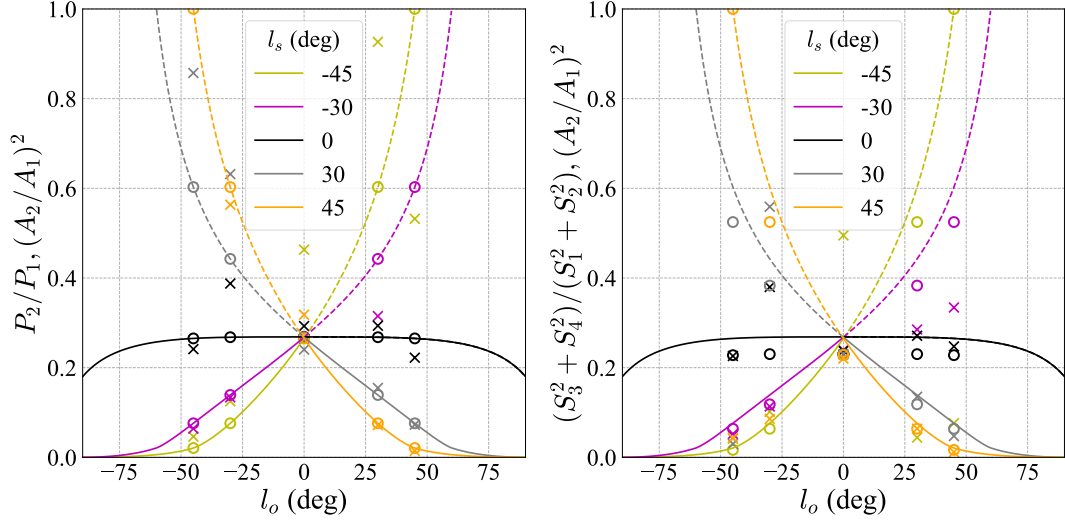


Fig. 14. Ratios of the second to fundamental Fourier coefficients for a single spot. Theoretical predictions $(A_2/A_1)^2$ for $\ell_s = -45^\circ$ (green yellow), -30° (purple), 0° (green), 30° (gray), and 45° (orange) are plotted against ℓ_o in solid ($\ell_s \ell_o \geq 0$) and dashed ($\ell_s \ell_o < 0$) lines. Open circles and crosses indicate the ratios estimated from the mock lightcurves for $b_{\text{spot}} \approx 85$ ppm with $\sigma = 0$, and 35 ppm, respectively. Left and right panels plot the result based on the Fourier power spectrum and the LS analysis with $n_{\text{terms}} = 2$.

by setting $\omega = \omega_{\text{fit}}$, and obtain the Fourier coefficients S_1 , S_2 , S_3 , and S_4 simultaneously. The symbols in the right panel plot the ratio $(S_3^2 + S_4^2)/(S_1^2 + S_2^2)$.

In the noiseless case, the Fourier power spectrum recovers the theoretical predictions very well, but the LS analysis seems to slightly but systematically underestimate the theoretical values. We do not understand why, but the fit to equation (31) with $n_{\text{terms}} = 2$ might be too restrictive and thus very sensitive to the best-fit value of ω_{fit} estimated from that with $n_{\text{terms}} = 1$.

In any case, the ratios estimated for data with $\sigma_n = 35$ ppm are not so accurate especially when the latitude of the spot is significantly different from the observer's line-of-sight (with different signs of ℓ_s and ℓ_o , for instance). Therefore, Figure 14 implies that it is possible to constrain ℓ_s and ℓ_o from the harmonic amplitude ratio for a single spot at least for $\sigma_n = 35$ ppm. For multi-spots cases, however, we find that the amplitude ratio varies significantly due to the differential rotation. Thus this methodology seems to be useful to constrain the spot parameter only when the photometric signal is dominated by a single prominent region.

3.4 Photometric rotation period for differentially rotating stars

Time-dependent distribution of multi-spots over a stellar surface leads to complex photometric modulation signals. Combined with the effect of latitudinal differential rotation, the peak of the rotation period would vary at different observing epochs. In turn, the variation of the rotation

period among different quarters may constrain the degree of the differential rotation.

In order to examine to what extent such signatures are indeed detectable from the Kepler data, we perform the LS analysis for seven different sets of mock data and plot distribution of the peak rotation period $P_{\text{rot,LS}}$ in Figure 15. Basically we adopt the fiducial values for parameters in Table 1; the equatorial rotation period of 10 days, $N_{\text{tot}} = 30$ spots following the Weibull distribution with $k = 0.54$ and $\lambda = 2.88\mu\text{Hem}$, the cadence of $T_{\text{samp}} = 30$ mins over an observing period of $T_{\text{obs}} = 90$ days corresponding to one quarter of the Kepler long-cadence data. The latitude of the observer’s line-of-sight ℓ_o and the range of the spot latitude $\ell_{s,\text{max}}$ are indicated in each panel.

The left panel of Figure 15 shows the histograms of the identified rotation period $P_{\text{rot,LS}}$, while the right panel plots histograms of the corresponding harmonic amplitude ratio $(A_2/A_1)^2$. Each histogram for seven models is computed from 300 realizations. The first three panels (a), (b) and (c) assume the differential rotation law and spot pattern similar to the Sun. They use the same 300 realizations of the spot pattern over $-30^\circ \leq \ell_s \leq 30^\circ$, but viewed from $\ell_o = 0^\circ$, 45° , and 75° , respectively. Similarly, panels (d) and (e) share the same set of 300 realizations with $-75^\circ \leq \ell_s \leq 75^\circ$ but viewed from $\ell_o = 0^\circ$ and 45° , respectively.

According to equation (2), the rotation period of the surface is longer than its equatorial value (10 days), and the width of the distribution reflects the observed range of the spot latitudes ℓ_s and the values of α_2 and α_4 .

Difference among panels (a), (b), and (c) is simply due to the fact that the observer at higher ℓ_o preferentially sees the spots located at higher ℓ_s as clearly illustrated in Figures 3, 4, and 5. Since the rotation periods estimated by observers at high ℓ_o should be dominated by a small number of big spots around $\ell_s > 0^\circ$, their distribution is shifted towards the larger $P_{\text{rot,LS}}$ due to the differential rotation, and the corresponding amplitude ratio becomes smaller as qualitatively expected from Figure 14. A fraction of spot patterns may exhibit an approximate symmetry between φ_s and $\varphi_s + \pi$ by chance, which would be interpreted as $P_{\text{rot,LS}} = 5$ days. Such symmetric patterns are more likely to be visible from the edge-on view ($\ell_o = 0^\circ$), which explains the fraction of the second peak around $P_{\text{rot,LS}} = 5$ days in panels (a), (b) and (c).

The next two panels (d) and (e) consider the case for the broader spot distribution over $-75^\circ \leq \ell_s \leq 75^\circ$. Because of the presence of a few spots located at higher latitudes, the differential rotation becomes more important, and the distribution of $P_{\text{rot,LS}}$ becomes even broader towards its larger value.

The last two panels are shown just for comparison purpose; panel (f) is for the stronger differential rotation case ($\alpha_2 = 3\alpha_{2\odot}$ and $\alpha_4 = 3\alpha_{4\odot}$), and panel (g) is for rigid rotation. Given

the same spot distribution pattern, comparison among panels (a), (f) and (g) indicates how the differential rotation law affects the distribution of the rotation period at different quarters of the Kepler data, for instance. This is expected to be directly applicable to put statistical constraints on the degree of latitudinal differential rotation of a population of stars, or to estimate the parameter α_2 (and even α_4) for stars exhibiting clear photometric lightcurve modulations.

While the harmonic ratios shown in the right panels reflect the statistical distribution of the spot latitudes to some extent, they are sensitive to the spot area distribution and do not seem to provide quantitatively useful information. Nevertheless, the histograms are qualitatively consistent with the expected range of the ratios plotted as the vertical dotted lines.

4 Summary and conclusion

We have presented an analytic model of the lightcurve variation due to starspots on a differentially rotating surface. If the dynamics of the spots over the timescale of the observing period is neglected, the Fourier coefficients of the harmonics of the rotation period are written primarily in terms of the latitude of spots and the observer’s line-of-sight direction angle.

In order to understand the resulting lightcurve variations, we generate various realizations of starspots according to the analytic model, and compute the Lomb-Scargle power spectra for the mock datasets.

Even though our analytical model neglects the evolution of spots on the stellar surface (dynamical motion, creation and annihilation), its prediction provides a useful framework to interpret the photometric variation of stars, in particular from the existing Kepler data and the future space-born mission. The conclusion and implications of the paper are summarized below.

1) If a photometric lightcurve of a star exhibits a clear single peak in the LS periodogram, the star may be well approximated as a rigid rotator, and the peak should correspond to the rotation period.

2) For those stars that have multiple peaks in the LS periodogram, the distribution of the peaks estimated in different quarters may be used to put constraints on parameters characterizing the differential rotation law.

3) In principle, the ratio of harmonics for the rotation period may constrain the spot latitude ℓ_s and stellar inclination ℓ_o given a limb darkening law. The constraint, however, is sensitive to the spot distribution, and seems to be useful only for a single spot dominated

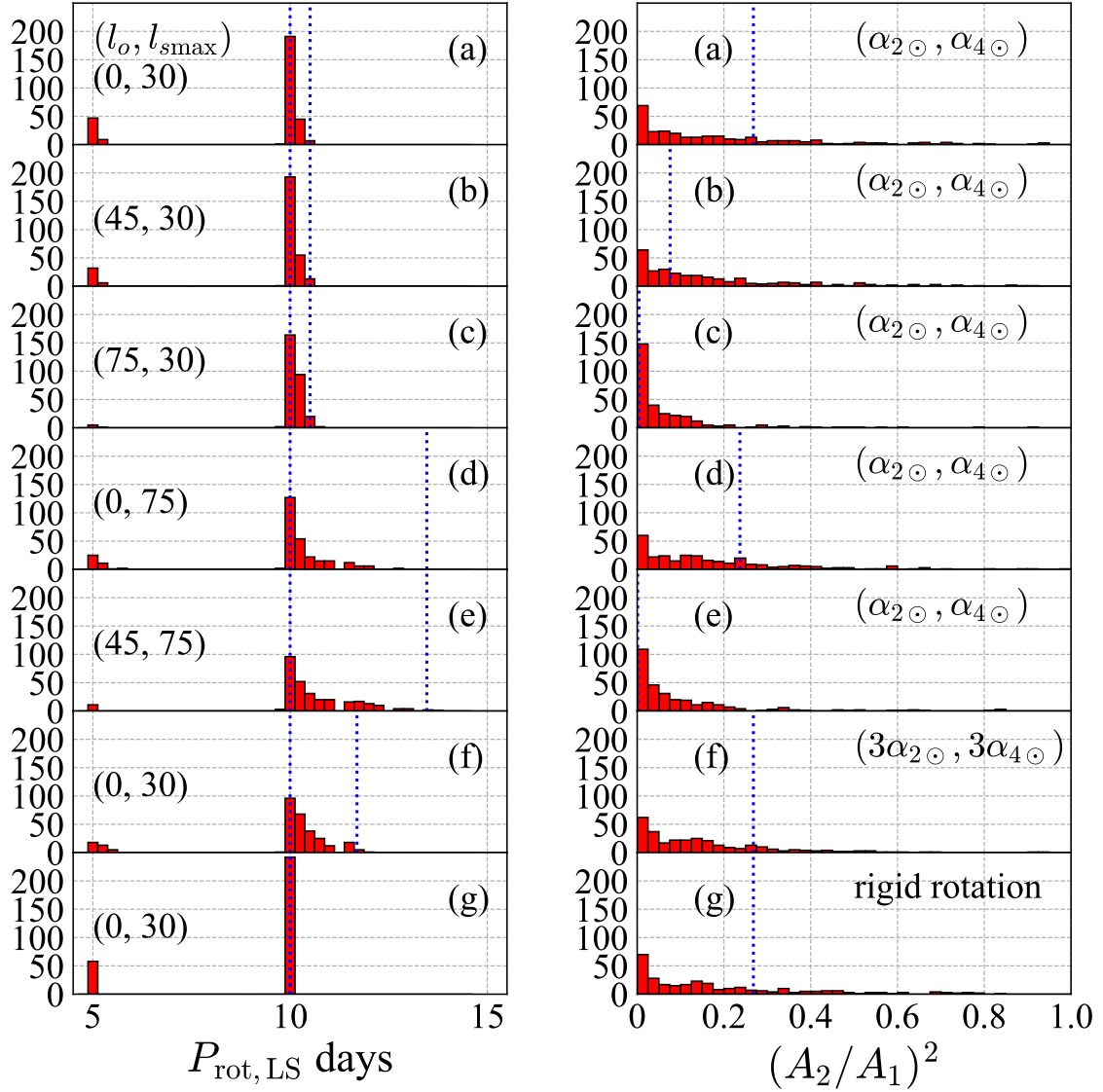


Fig. 15. Distribution of the photometric rotation period and the Fourier coefficient ratio estimated from 300 realizations of $N_{\text{tot}} = 30$ spots with $\sigma_n = 35\text{ppm}$. We adopt the fiducial parameter set of the equatorial rotation period 10 days, $T_{\text{samp}} = 30$ mins, $T_{\text{obs}} = 90$ days. We compute the histograms by varying the observer's line-of-sight, and the range of the spot latitudes $-\ell_{s, \text{max}} < \ell_s < \ell_{s, \text{max}}$, and the differential rotation parameters, which are indicated in each panel. Vertical dotted lines indicate the range of the differentially rotation periods as in Figure 7 (left panels), and the predicted ratio for $\ell_{s, \text{max}}$ (right panels). Panels (a), (b) and (c) use the same set of 300 realizations but viewed from the different observer's latitudes.

case. Nevertheless, joint analysis with independent constraints on ℓ_o from spectroscopic and/or asteroseismic measurements may improve the constraint. We have not explored this possibility in the present paper, but it is worthwhile to pursue in future.

4) The analytical model presented in the paper is based on the distribution of the *effective* area of spots b_{spot} alone, and does not require the information of the geometric area and temperature simultaneously. Thus it is applicable not only for spots on main-sequence stars, but for other inhomogeneities on rotating systems. For instance, the recent discovery of the fastest-period white dwarf (Kilic et al. 2021) indicates that the interpretation of the photometric modulation of white dwarfs is crucial in extracting their rotation period. Since it is likely to originate from the small hot spot around the polar region, the determination of ℓ_s and ℓ_o with respect to our line-of-sight may be more promising for white dwarfs than for stars with many different spots, as long as the modulation signal-to-noise ratio is sufficiently high.

The above findings may have numerous useful applications even in the existing Kepler data that cover a wide variety of stars with different properties of spots on their surface. We are currently working on the joint analysis of photometric and asteroseismic measurements of Kepler stars selected by Kamiaka et al. (2018), and plan to present the results elsewhere in due course (Y.Lu et al. in preparation).

Acknowledgements

We thank an anonymous referee for various constructive comments on the manuscript. Simulations and analyses in this paper made use of a community-developed core Python package for Astronomy, **Astropy**. This work is supported by Grants-in Aid for Scientific Research by the Japan Society for Promotion of Science (JSPS) No.18H012 and No.19H01947, and from JSPS Core-to-core Program “International Network of Planetary Sciences”.

References

- Albrecht, S. H., Marcussen, M. L., Winn, J. N., Dawson, R. I., & Knudstrup, E. 2021, ApJL, 916, L1
- Angus, R., Morton, T., Aigrain, S., Foreman-Mackey, D., & Rajpaul, V. 2018, MNRAS, 474, 2094
- Appourchaux, T., Michel, E., Auvergne, M., Baglin, A., Toutain, T., Baudin, F., Benomar, O., Chaplin, W. J., Deheuvels, S., Samadi, R., Verner, G. A., Boumier, P., García, R. A., Mosser, B., Hurlot, J.-C., Ballot, J., Barban, C., Elsworth, Y., Jiménez-Reyes, S. J., Kjeldsen, H., Régulo, C., & Roxburgh, I. W. 2008, A&A, 488, 705

- Baglin, A., Auvergne, M., Barge, P., Deleuil, M., Catala, C., Michel, E., Weiss, W., & COROT Team. 2006, in *ESA Special Publication*, Vol. 1306, *ESA Special Publication*, ed. M. Fridlund, A. Baglin, J. Lochard, & L. Conroy, 33
- Barnes, J. R., Collier Cameron, A., Donati, J.-F., James, D. J., Marsden, S. C., & Petit, P. 2005, *MNRAS*, 357, L1
- Basri, G. & Shah, R. 2020, *ApJ*, 901, 14
- Benomar, O., Bazot, M., Nielsen, M. B., Gizon, L., Sekii, T., Takata, M., Hotta, H., Hanasoge, S., Sreenivasan, K. R., & Christensen-Dalsgaard, J. 2018, *Science*, 361, 1231
- Benomar, O., Masuda, K., Shibahashi, H., & Suto, Y. 2014, *PASJ*, 66, 94
- Borucki, W. J., Koch, D., Basri, G., Batalha, N., Brown, T., Caldwell, D., Caldwell, J., Christensen-Dalsgaard, J., Cochran, W. D., DeVore, E., Dunham, E. W., Dupree, A. K., Gautier, T. N., Geary, J. C., Gilliland, R., Gould, A., Howell, S. B., Jenkins, J. M., Kondo, Y., Latham, D. W., Marcy, G. W., Meibom, S., Kjeldsen, H., Lissauer, J. J., Monet, D. G., Morrison, D., Sasselov, D., Tarter, J., Boss, A., Brownlee, D., Owen, T., Buzasi, D., Charbonneau, D., Doyle, L., Fortney, J., Ford, E. B., Holman, M. J., Seager, S., Steffen, J. H., Welsh, W. F., Rowe, J., Anderson, H., Buchhave, L., Ciardi, D., Walkowicz, L., Sherry, W., Horch, E., Isaacson, H., Everett, M. E., Fischer, D., Torres, G., Johnson, J. A., Endl, M., MacQueen, P., Bryson, S. T., Dotson, J., Haas, M., Kolodziejczak, J., Van Cleve, J., Chandrasekaran, H., Twicken, J. D., Quintana, E. V., Clarke, B. D., Allen, C., Li, J., Wu, H., Tenenbaum, P., Verner, E., Bruhweiler, F., Barnes, J., & Prsa, A. 2010, *Science*, 327, 977
- Brun, A. S., Strugarek, A., Varela, J., Matt, S. P., Augustson, K. C., Emeriau, C., DoCao, O. L., Brown, B., & Toomre, J. 2017, *ApJ*, 836, 192
- Chaplin, W. J., Appourchaux, T., Elsworth, Y., García, R. A., Houdek, G., Karoff, C., Metcalfe, T. S., Molenda-Żakowicz, J., Monteiro, M. J. P. F. G., Thompson, M. J., Brown, T. M., Christensen-Dalsgaard, J., Gilliland, R. L., Kjeldsen, H., Borucki, W. J., Koch, D., Jenkins, J. M., Ballot, J., Basu, S., Bazot, M., Bedding, T. R., Benomar, O., Bonanno, A., Brandão, I. M., Bruntt, H., Campante, T. L., Creevey, O. L., Di Mauro, M. P., Doğan, G., Dreizler, S., Eggenberger, P., Esch, L., Fletcher, S. T., Frandsen, S., Gai, N., Gaulme, P., Handberg, R., Hekker, S., Howe, R., Huber, D., Korzennik, S. G., Lebrun, J. C., Leccia, S., Martić, M., Mathur, S., Mosser, B., New, R., Quirion, P. O., Régulo, C., Roxburgh, I. W., Salabert, D., Schou, J., Sousa, S. G., Stello, D., Verner, G. A., Arentoft, T., Barban, C., Belkacem, K., Benatti, S., Biazzo, K., Boumier, P., Bradley, P. A., Broomhall, A. M., Buzasi, D. L., Claudi, R. U., Cunha, M. S., D’Antona, F., Deheuvels, S., Derekas, A., García Hernández, A., Giampapa, M. S., Goupil, M. J., Gruberbauer, M., Guzik, J. A., Hale, S. J., Ireland, M. J., Kiss, L. L., Kitiashvili, I. N., Kolenberg, K., Korhonen, H., Kosovichev, A. G.,

- Kupka, F., Lebreton, Y., Leroy, B., Ludwig, H. G., Mathis, S., Michel, E., Miglio, A., Montalbán, J., Moya, A., Noels, A., Noyes, R. W., Pallé, P. L., Piau, L., Preston, H. L., Roca Cortés, T., Roth, M., Sato, K. H., Schmitt, J., Serenelli, A. M., Silva Aguirre, V., Stevens, I. R., Suárez, J. C., Suran, M. D., Trampedach, R., Turck-Chièze, S., Uytterhoeven, K., Ventura, R., & Wilson, P. A. 2010, *ApJL*, 713, L169
- Christensen-Dalsgaard, J., Dappen, W., Ajukov, S. V., Anderson, E. R., Antia, H. M., Basu, S., Baturin, V. A., Berthomieu, G., Chaboyer, B., Chitre, S. M., Cox, A. N., Demarque, P., Donatowicz, J., Dziembowski, W. A., Gabriel, M., Gough, D. O., Guenther, D. B., Guzik, J. A., Harvey, J. W., Hill, F., Houdek, G., Iglesias, C. A., Kosovichev, A. G., Leibacher, J. W., Morel, P., Proffitt, C. R., Provost, J., Reiter, J., Rhodes, Jr., E. J., Rogers, F. J., Roxburgh, I. W., Thompson, M. J., & Ulrich, R. K. 1996, *Science*, 272, 1286
- Cox, A. N. 2000, *Allen’s astrophysical quantities*, 4th edn. (Springer–Verlag)
- Donati, J.-F. & Collier Cameron, A. 1997, *MNRAS*, 291, 1
- Donati, J.-F., Skelly, M. B., Bouvier, J., Jardine, M. M., Gregory, S. G., Morin, J., Hussain, G. A. J., Dougados, C., Ménard, F., & Unruh, Y. 2010, *MNRAS*, 402, 1426
- Dorren, J. D. 1987, *ApJ*, 320, 756
- Farr, B., Farr, W. M., Cowan, N. B., Haggard, H. M., & Robinson, T. 2018, *AJ*, 156, 146
- Fujii, Y., Kawahara, H., Suto, Y., Fukuda, S., Nakajima, T., Livengood, T. A., & Turner, E. L. 2011, *ApJ*, 738, 184
- Fujii, Y., Kawahara, H., Suto, Y., Taruya, A., Fukuda, S., Nakajima, T., & Turner, E. L. 2010, *ApJ*, 715, 866
- Haggard, H. M. & Cowan, N. B. 2018, *MNRAS*, 478, 371
- Hirano, T., Sanchis-Ojeda, R., Takeda, Y., Narita, N., Winn, J. N., Taruya, A., & Suto, Y. 2012, *ApJ*, 756, 66
- Huber, D., Chaplin, W. J., Christensen-Dalsgaard, J., Gilliland, R. L., Kjeldsen, H., Buchhave, L. A., Fischer, D. A., Lissauer, J. J., Rowe, J. F., Sanchis-Ojeda, R., Basu, S., Handberg, R., Hekker, S., Howard, A. W., Isaacson, H., Karoff, C., Latham, D. W., Lund, M. N., Lundkvist, M., Marcy, G. W., Miglio, A., Silva Aguirre, V., Stello, D., Arentoft, T., Barclay, T., Bedding, T. R., Burke, C. J., Christiansen, J. L., Elsworth, Y. P., Haas, M. R., Kawaler, S. D., Metcalfe, T. S., Mullally, F., & Thompson, S. E. 2013, *ApJ*, 767, 127
- Kamiaka, S., Benomar, O., & Suto, Y. 2018, *MNRAS*, 479, 391
- Kamiaka, S., Benomar, O., Suto, Y., Dai, F., Masuda, K., & Winn, J. N. 2019, *AJ*, 157, 137
- Kawaler, S. D. 1988, *ApJ*, 333, 236

- Kilic, M., Kosakowski, A., Moss, A. G., Bergeron, P., & Conly, A. A. 2021, arXiv e-prints, arXiv:2111.14902
- Kjeldsen, H. & Bedding, T. R. 1995, *A&A*, 293, 87
- Lomb, N. R. 1976, *Astrophysics and Space Science*, 39, 447
- Louden, E. M., Winn, J. N., Petigura, E. A., Isaacson, H., Howard, A. W., Masuda, K., Albrecht, S., & Kosiarek, M. R. 2021, *AJ*, 161, 68
- Lund, M. N., Silva Aguirre, V., Davies, G. R., Chaplin, W. J., Christensen-Dalsgaard, J., Houdek, G., White, T. R., Bedding, T. R., Ball, W. H., Huber, D., Antia, H. M., Lebreton, Y., Latham, D. W., Handberg, R., Verma, K., Basu, S., Casagrande, L., Justesen, A. B., Kjeldsen, H., & Mosumgaard, J. R. 2017, *ApJ*, 835, 172
- MacGregor, K. & Brenner, M. 1991, *ApJ*, 376, 204
- Mandal, S., Krivova, N. A., Cameron, R., & Solanki, S. K. 2021, *A&A*, 652, A9
- Maunder, E. W. 1904, *MNRAS*, 64, 747
- Mazeh, T., Perets, H. B., McQuillan, A., & Goldstein, E. S. 2015, *ApJ*, 801, 3
- McQuillan, A., Mazeh, T., & Aigrain, S. 2014, *ApJS*, 211, 24
- Morris, B. M. 2020, *ApJ*, 893, 67
- Muñoz-Jaramillo, A., Senkpeil, R. R., Windmueller, J. C., Amouzou, E. C., Longcope, D. W., Tlatov, A. G., Nagovitsyn, Y. A., Pevtsov, A. A., Chapman, G. A., Cookson, A. M., Yeates, A. R., Watson, F. T., Balmaceda, L. A., DeLuca, E. E., & Martens, P. C. H. 2015, *ApJ*, 800, 48
- Nakagawa, Y., Kodama, T., Ishiwatari, M., Kawahara, H., Suto, Y., Takahashi, Y. O., Hashimoto, G. L., Kuramoto, K., Nakajima, K., Takehiro, S.-i., & Hayashi, Y.-Y. 2020, *ApJ*, 898, 95
- Ohta, Y., Taruya, A., & Suto, Y. 2005, *ApJ*, 622, 1118
- Ossendrijver, M. 2003, *A&AR*, 11, 287
- Queloz, D., Eggenberger, A., Mayor, M., Perrier, C., Beuzit, J. L., Naef, D., Sivan, J. P., & Udry, S. 2000, *A&A*, 359, L13
- Ricker, G. R., Winn, J. N., Vanderspek, R., Latham, D. W., Bakos, G. Á., Bean, J. L., Bert-Thompson, Z. K., Brown, T. M., Buchhave, L., Butler, N. R., Butler, R. P., Chaplin, W. J., Charbonneau, D., Christensen-Dalsgaard, J., Clampin, M., Deming, D., Doty, J., De Lee, N., Dressing, C., Dunham, E., Endl, M., Fressin, F., Ge, J., Henning, T., Holman, M. J., Howard, A. W., Ida, S., Jenkins, J., Jernigan, G., Johnson, J. A., Kaltenegger, L., Kawai, N., Kjeldsen, H., Laughlin, G., Levine, A. M., Lin, D., Lissauer, J. J., MacQueen, P., Marcy, G., McCullough, P., Morton, T. D., Narita, N., Paegert, M., Palte, E., Pepe, F., Pepper, J., Quirrenbach, A., Rinehart, S., Sasselov, D., Sato, B., Seager, S., Sozzetti, A., Stassun, K. G., Sullivan, P., Szentgyorgyi, A.,

- Torres, G., Udry, S., & Villaseñor, J. 2014, in Society of Photo-Optical Instrumentation Engineers (SPIE) Conference Series, Vol. 9143, \procspie, 914320
- Roettenbacher, R. M., Monnier, J. D., Harmon, R. O., Barclay, T., & Still, M. 2013, ApJ, 767, 60
- Sanchis-Ojeda, R. & Winn, J. N. 2011, ApJ, 743, 61
- Sanchis-Ojeda, R., Winn, J. N., Holman, M. J., Carter, J. A., Osip, D. J., & Fuentes, C. I. 2011, ApJ, 733, 127
- Sasaki, S. & Suto, Y. 2021, PASJ, 73, 1656
- Scargle, J. D. 1982, ApJ, 263, 835
- Skumanich, A. 1972, ApJ, 171, 565
- Snodgrass, H. B. & Ulrich, R. K. 1990, ApJ, 351, 309
- van Saders, J., Ceillier, T., Metcalfe, T., Silva Aguirre, V., Pinsonneault, M., García, R., Mathur, S., & Davies, G. 2016, Nature, 529, 181
- Varela, J., Strugarek, A., & Brun, A. 2016, Advances in Space Research, 58, 1507
- Walker, G., Matthews, J., Kuschnig, R., Johnson, R., Rucinski, S., Pazder, J., Burley, G., Walker, A., Skaret, K., Zee, R., Grocott, S., Carroll, K., Sinclair, P., Sturgeon, D., & Harron, J. 2003, PASP, 115, 1023
- Walkowicz, L. M., Basri, G., & Valenti, J. A. 2013, ApJS, 205, 17
- Zharkov, S., Zharkova, V. V., & Ipson, S. S. 2005, Sol. Phys., 228, 377

Appendix 1 Fourier series expansion for spots with $|\Gamma| < 1$

The present paper is based on the analytic Fourier series expansion of the photometric lightcurve due to a single spot. Those expressions are derived in this appendix.

We first compute the Fourier expansion of equation (8) by setting

$$F_1(t) \equiv \max(\cos \omega_s t + \Gamma, 0) = \frac{a_0}{2} + \sum_{n=1}^{\infty} a_n \cos n \omega_s t. \quad (\text{A1})$$

Thus, the coefficients a_n are simply given by

$$a_n = \frac{\omega_s}{\pi} \int_{-\pi/\omega_s}^{+\pi/\omega_s} \max(\cos \omega_s t + \Gamma, 0) \cos n \omega_s t dt. \quad (\text{A2})$$

It is convenient to introduce the angle θ_c for $|\Gamma| < 1$ through

$$\Gamma \equiv -\cos \theta_c \quad (0 < \theta_c < \pi). \quad (\text{A3})$$

Then, equation (A2) reduces to

$$a_n = \frac{2}{\pi} \int_0^{\theta_c} (\cos \theta - \cos \theta_c) \cos n \theta d\theta$$

$$= \frac{1}{\pi} \int_0^{\theta_c} [\cos(n+1)\theta + \cos(n-1)\theta] d\theta - \frac{2}{\pi} \cos\theta_c \int_0^{\theta_c} \cos n\theta d\theta. \quad (\text{A4})$$

The straightforward integration of equation (A4) yields

$$\frac{a_0}{2} = \frac{1}{\pi} (\sin\theta_c - \theta_c \cos\theta_c), \quad (\text{A5})$$

$$a_1 = \frac{1}{2\pi} (2\theta_c - \sin 2\theta_c), \quad (\text{A6})$$

$$a_n = \frac{1}{n\pi} \left[\frac{\sin(n-1)\theta_c}{n-1} - \frac{\sin(n+1)\theta_c}{n+1} \right] \quad (n \geq 2), \quad (\text{A7})$$

which are a set of coefficients shown in equation (12) of the main text.

If the limb darkening effect is considered, one has to compute two additional expansions including

$$F_2(t) \equiv [\max(\cos\omega_s t + \Gamma, 0)]^2 = \frac{b_0}{2} + \sum_{n=1}^{\infty} b_n \cos n\omega_s t, \quad (\text{A8})$$

and

$$F_3(t) \equiv [\max(\cos\omega_s t + \Gamma, 0)]^3 = \frac{c_0}{2} + \sum_{n=1}^{\infty} c_n \cos n\omega_s t. \quad (\text{A9})$$

Similarly to equation (A4), the coefficients b_n and c_n are given as

$$b_n = \frac{2}{\pi} \int_0^{\theta_c} (\cos\theta - \cos\theta_c)^2 \cos n\theta d\theta, \quad (\text{A10})$$

and

$$c_n = \frac{2}{\pi} \int_0^{\theta_c} (\cos\theta - \cos\theta_c)^3 \cos n\theta d\theta. \quad (\text{A11})$$

After tedious but straightforward calculations, we obtain

$$\frac{b_0}{2} = \frac{1}{\pi} \left(\theta_c + \frac{\theta_c}{2} \cos 2\theta_c - \frac{3}{4} \sin 2\theta_c \right), \quad (\text{A12})$$

$$b_1 = \frac{2}{\pi} \left(-\theta_c \cos\theta_c - \frac{3}{4} \sin\theta_c + \frac{1}{12} \sin 3\theta_c \right), \quad (\text{A13})$$

$$b_2 = \frac{2}{\pi} \left(\frac{\theta_c}{4} - \frac{1}{6} \sin 2\theta_c + \frac{1}{48} \sin 4\theta_c \right), \quad (\text{A14})$$

$$b_n = \frac{1}{2n\pi} \left[\frac{\sin(n-2)\theta_c}{(n-1)(n-2)} - \frac{2\sin n\theta_c}{(n-1)(n+1)} + \frac{\sin(n+2)\theta_c}{(n+1)(n+2)} \right] \quad (n \geq 3), \quad (\text{A15})$$

and

$$\frac{c_0}{2} = \frac{1}{\pi} \left(-\frac{9\theta_c}{4} \cos\theta_c + \frac{9}{8} \sin\theta_c - \frac{\theta_c}{4} \cos 3\theta_c + \frac{11}{24} \sin 3\theta_c \right), \quad (\text{A16})$$

$$c_1 = \frac{2}{\pi} \left(\frac{9}{8} \theta_c + \frac{3\theta_c}{4} \cos 2\theta_c - \frac{7}{8} \sin 2\theta_c - \frac{1}{32} \sin 4\theta_c \right), \quad (\text{A17})$$

$$c_2 = \frac{2}{\pi} \left(-\frac{3\theta_c}{4} \cos\theta_c + \frac{1}{2} \sin\theta_c - \frac{3}{32} \sin 3\theta_c - \frac{1}{160} \sin 5\theta_c \right), \quad (\text{A18})$$

$$c_3 = \frac{2}{\pi} \left(\frac{1}{8} \theta_c - \frac{3}{32} \sin 2\theta_c + \frac{3}{160} \sin 4\theta_c - \frac{1}{480} \sin 6\theta_c \right), \quad (\text{A19})$$

$$c_n = \frac{3}{4n\pi} \left[\frac{\sin(n-3)\theta_c}{(n-1)(n-2)(n-3)} - \frac{3\sin(n-1)\theta_c}{(n-1)(n+1)(n-2)} + \frac{3\sin(n+1)\theta_c}{(n-1)(n+1)(n+2)} - \frac{\sin(n+3)\theta_c}{(n+1)(n+2)(n+3)} \right] \quad (n \geq 4). \quad (\text{A20})$$

The above coefficients are combined and form the coefficients A_n in equation (18) of the main text:

$$A_n \equiv (1 - u_1 - u_2)(\cos \ell_o \cos \ell_s) a_n + (u_1 + 2u_2)(\cos \ell_o \cos \ell_s)^2 b_n - u_2(\cos \ell_o \cos \ell_s)^3 c_n. \quad (\text{A21})$$

Appendix 2 Fourier series expansion for spots with $\Gamma > 1$

For those spots with $\Gamma > 1$, the coefficients A_n for spots with $|\Gamma| < 1$ should be replaced by \tilde{A}_n , which are defined through

$$\mu_s I(\mu_s) = \frac{\tilde{A}_0}{2} + \sum_{n=1}^{\infty} \tilde{A}_n \cos n\omega_s t, \quad (\text{A22})$$

where

$$\mu_s = \cos \ell_o \cos \ell_s (\cos \omega_s t + \Gamma), \quad (\text{A23})$$

$$I(\mu) = 1 - u_1(1 - \mu) - u_2(1 - \mu)^2 = (1 - u_1 - u_2) + (u_1 + 2u_2)\mu - u_2\mu^2. \quad (\text{A24})$$

Unlike in Appendix 1, the left-hand-side of equation (A22) is explicitly written in terms of up to the third-order polynomials of $\cos \omega_s t$. Thus, \tilde{A}_n can be explicitly given in the following forms:

$$\begin{aligned} \frac{\tilde{A}_0}{2} = & (1 - u_1 - u_2)(\cos \ell_o \cos \ell_s) \Gamma + (u_1 + 2u_2)(\cos \ell_o \cos \ell_s)^2 \left(\Gamma^2 + \frac{1}{2} \right) \\ & - u_2(\cos \ell_o \cos \ell_s)^3 \left(\Gamma^3 + \frac{3\Gamma}{2} \right), \end{aligned} \quad (\text{A25})$$

$$\begin{aligned} \tilde{A}_1 = & (1 - u_1 - u_2)(\cos \ell_o \cos \ell_s) + 2(u_1 + 2u_2)(\cos \ell_o \cos \ell_s)^2 \Gamma \\ & - u_2(\cos \ell_o \cos \ell_s)^3 \left(3\Gamma^2 + \frac{3}{4} \right), \end{aligned} \quad (\text{A26})$$

$$\tilde{A}_2 = \frac{u_1 + 2u_2}{2} (\cos \ell_o \cos \ell_s)^2 \Gamma - u_2(\cos \ell_o \cos \ell_s)^3 \frac{3\Gamma}{2}, \quad (\text{A27})$$

$$\tilde{A}_3 = -\frac{u_2}{4} (\cos \ell_o \cos \ell_s)^3, \quad (\text{A28})$$

$$\tilde{A}_n = 0 \quad (n \geq 4). \quad (\text{A29})$$